



A Collage of Small Planets from the Lick–Carnegie Exoplanet Survey: Exploring the Super-Earth and Sub-Neptune Mass Regime*

Jennifer Burt¹ , Fabo Feng^{2,3} , Bradford Holden⁴ , Eric E. Mamajek⁵ , Chelsea X. Huang^{6,14} , Mickey M. Rosenthal⁷ , Songhu Wang⁸ , R. Paul Butler⁹ , Steven S. Vogt⁴ , Gregory Laughlin¹⁰ , Gregory W. Henry¹¹ , Johanna K. Teske^{9,15} , Sharon X. Wang¹² , Jeffrey D. Crane¹³ , and Steve A. Sheckman¹³ 

¹ Jet Propulsion Laboratory, California Institute of Technology, 4800 Oak Grove drive, Pasadena CA 91109, USA; jennifer.burt@jpl.nasa.gov

² Tsung-Dao Lee Institute, Shanghai Jiao Tong University, 800 Dongchuan Road, Shanghai 200240, People's Republic of China

³ Department of Astronomy, School of Physics and Astronomy, Shanghai Jiao Tong University, 800 Dongchuan Road, Shanghai 200240, People's Republic of China

⁴ UCO/Lick Observatory, Department of Astronomy and Astrophysics, University of California at Santa Cruz, Santa Cruz, CA 95064, USA

⁵ Jet Propulsion Laboratory, California Institute of Technology, 4800 Oak Grove Drive, Pasadena, CA 91109, USA

⁶ Department of Physics and Kavli Institute for Astrophysics and Space Research, Massachusetts Institute of Technology, Cambridge, MA 02139, USA

⁷ Department of Astronomy and Astrophysics, University of California, Santa Cruz, CA 95064, USA

⁸ Department of Astronomy, Indiana University, Bloomington, IN 47405, USA

⁹ Earth and Planets Laboratory, Carnegie Institution for Science, 5241 Broad Branch Road, NW, Washington, DC 20015, USA

¹⁰ Department of Astronomy, Yale University, New Haven, CT 06511, USA

¹¹ Center of Excellence in Information Systems, Tennessee State University, Nashville, TN 37209, USA

¹² Department of Astronomy, Tsinghua University, Beijing 100084, People's Republic of China

¹³ Observatories of the Carnegie Institution for Science, 813 Santa Barbara Street, Pasadena, CA 91101, USA

Received 2020 April 30; revised 2020 October 4; accepted 2020 October 13; published 2020 December 3

Abstract

Analysis of new precision radial velocity (RV) measurements from the Lick Automated Planet Finder and Keck HIRES has yielded the discovery of three new exoplanet candidates orbiting the nearby stars HD 190007 and HD 216520. We also report new velocities from the APF and the Planet Finder Spectrograph and updated orbital fits for the known exoplanet host stars GJ 686 and HD 180617. Of the newly discovered planets, HD 190007 b has a period of $P = 11.72$ days, an RV semiamplitude of $K = 5.64 \pm 0.55 \text{ m s}^{-1}$, a minimum mass of $M_{\text{pl}} = 16.46 \pm 1.66 M_{\oplus}$, and orbits the slightly metal-rich, active K4V star HD 190007. For HD 216520 b, we find $P = 35.45$ days, $K = 2.28 \pm 0.20 \text{ m s}^{-1}$, and $M_{\text{pl}} = 10.26 \pm 0.99 M_{\oplus}$, while for HD 216520 c, $P = 154.43$ days, $K = 1.29 \pm 0.22 \text{ m s}^{-1}$, and $M_{\text{pl}} = 9.44 \pm 1.63 M_{\oplus}$. Both planets orbit the slightly metal-poor, inactive K0V star HD 216520. Our updated best-fit models for HD 180617 b and GJ 686 b are in good agreement with the published results. For HD 180617 b, we obtain $P = 105.91$ days and $M_{\text{pl}} = 12.214 \pm 1.05 M_{\oplus}$. For GJ 686 b, we find $P = 15.53$ days and $M_{\text{pl}} = 6.624 \pm 0.432 M_{\oplus}$. Using an injection-recovery exercise, we find that HD 190007 b and HD 216520 b are unlikely to have additional planets with masses and orbital periods within a factor of 2, in marked contrast to $\sim 85\%$ of planets in this mass and period range discovered by Kepler.

Unified Astronomy Thesaurus concepts: [Exoplanet astronomy \(486\)](#); [Exoplanet detection methods \(489\)](#); [Exoplanets \(498\)](#); [Radial velocity \(1332\)](#); [Mini Neptunes \(1063\)](#)

Supporting material: machine-readable tables

1. Introduction

The use of precision ground-based Doppler spectrometers enabled the first generation of exoplanet detections, producing 47 exoplanet detections before the first exoplanet was discovered to transit in 1999 (Henry et al. 1999, 2000). Since then, an additional 773 planets have been discovered using such instruments, bringing the total number of radial velocity (RV) detected planets to 820 as of 2020 September.¹⁶

More recently, numerous precision RV instruments have been spending more time pursuing targeted mass measurements of transiting planets discovered by space-based missions like K2 and TESS. Such planets, for which we can obtain both mass and radius measurements, are valuable additions to the field as they enable studies of planetary composition and evolution (see, e.g., Christiansen et al. 2017; Teske et al. 2018, Burt et al. 2020).

However, more traditional Doppler surveys, which focus on repeated observations of nearby stars without any a priori knowledge of whether or not they host planets, are still a key component in our efforts to understand the Galaxy's exoplanet population. Because RV detections do not require an exoplanet to transit its host star, an alignment that happens with only a few percent probability for even promising short-period planets (Winn 2010), this method is sensitive to a wider range of orbital configurations. As such, many of our constraints on the characteristics and occurrence rates of long-period gas and ice giant planets come from RV surveys (Rowan et al. 2016; Bryan et al. 2019). And unlike transit observations, which detect planets during their fleeting inferior conjunctions, RV observations permit the planetary signal to build in the data over the entire span of observing time so that they do not suffer as badly from short-term weather closures or varied observing times/locations. Examples of such surveys include the Lick–Carnegie Exoplanet Survey (LCES; Butler et al. 2017, hereafter B17), the California Planet Search (CPS; Howard et al. 2010), the HARPS search for southern extrasolar planets (Pepe et al. 2004), and the CARMENES search for exoplanets around M dwarfs (Reiners et al. 2018).

* This paper includes data gathered with the 6.5 m Magellan Telescopes located at Las Campanas Observatory, Chile.

¹⁴ Juan Carlos Torres Fellow.

¹⁵ NASA Hubble Fellow.

¹⁶ <https://exoplanetarchive.ipac.caltech.edu>

While they are less susceptible to short-term disruptions, RV surveys are more observationally expensive than transit surveys, requiring both long exposure times to reach the required high signal-to-noise ratio (S/N) levels on high-resolution spectrometers and long observing baselines to properly fill out a planet’s RV phase curve. This combination means that surveys often require months or years of data on a star before any potential planet signals are interpreted as robust detections. Additionally, RV surveys can often begin by selecting stars that seem promising based on their V magnitudes, effective temperatures (T_{eff}), rotational velocities, and $\log R'_{\text{HK}}$ activity indicators, only to learn months or years later that the stars are actually too active to allow for the detection of Keplerian signals that are only a few m s^{-1} in amplitude. When such stars are ultimately dropped from a survey, however, there is often no public record of the discontinuation of RV monitoring, nor is there a write up of why the star was excluded. This can result in future surveys observing that same target again and spending many nights of telescope time only to realize once again that the star is not well suited to RV science. Dropping targets also has strong, detrimental impacts on efforts to infer RV planet population statistics and makes it difficult to draw robust conclusions about planet occurrence rates from most RV surveys.

In 2017, the LCES team released a compendium of all the Keck HIRES RV observations acquired since the advent of the survey in 1994, resulting in 64,949 radial velocities spread over 1624 stars in B17. The majority of stars included in the survey have V magnitudes between 6 and 10, with a median value of $V = 8$. Stars brighter than 5th mag were handled by the Hamilton spectrograph on the Shane 3 m telescope at Lick Observatory. Observing times were limited to roughly 10 minutes per target per night in order to accommodate a relatively large target list, which led to a faint magnitude limit of about 14th mag. The stellar spectral types covered by the survey run from about F5V to M6V. Stars hotter than F5V were generally avoided due to the decrease in RV information content (Bouchy et al. 2001; Beatty & Gaudi 2015) while stars cooler than M6V were generally past the faint end of the survey’s magnitude limit. For new or ongoing planet search surveys, the ability to sift through two decades of archival data and use it for either initial target selection or in combination with recent RV observations to search for potential Keplerian signals (or trends that could indicate notable stellar activity cycles which can last many years) is a powerful tool.

In this work, we make use of the LCES RV catalog as the backbone for two new planet detections and updated fits for two recently published planets. Two of these stars are among the 357 found in B17 to have significant signals that are of constant period and phase, but not coincident in period and/or phase with stellar activity indices in the original catalog publication. The other two display significant RV periodicities only after the HIRES velocities have been combined with RV data from other observatories. We begin in Section 2 with an overview of the specifics of each step of our analysis methods, as they are shared between the four stellar data sets. Then we detail the characteristics of exoplanet host stars and present a compilation of their stellar parameters in Section 3. Next, we cover each star and its associated planet detection individually in Sections 4–7 before concluding in Section 8 with a discussion about how these planets compare to the multiplanet systems discovered in large part by the Kepler mission.

2. Overview of Data and Methodology

Each star is analyzed using the same methodology and series of steps, which we summarize here. The initial data product for each target is a set of time series RV measurements and the corresponding spectral activity indicators from various PRV instruments which are monitored using the interactive SYSTEMIC Console (Meschiari et al. 2009) over the months/years that the stars spend on our survey target lists. When the RV data sets show signs of a significant signal, we then work to determine whether or not the signal could have been caused by our observing approach or by the host star itself via chromospheric activity and/or stellar rotation (see, e.g., Rajpaul et al. 2016). To this end, we first compute the spectral window function of the RV data sets to ensure the signal is not due to our observational cadence. We then gather, when available, long-baseline photometric measurements to try and measure the stars’ rotation periods via seasonal changes in stellar brightness. We also derive S - and H -index activity indicators (described in Section 2.4) from the RV spectra to map the stars’ chromospheric activity signatures. And finally, we assess the consistency of any signals over time by computing a moving periodogram with a moving average noise model (MA(1) model, described in Section 2.3) for those signals whose orbital phases are well covered by the RV data. If none of these analyses produce signals that can explain the signature seen in the RV data, we then test whether the signal originally noted with SYSTEMIC is “significant” under a full Bayesian treatment as seen in Feng et al. (2019). If so, we assume the signal is caused by a planet in orbit around the host star and fit a Keplerian model to determine the exact parameters of the planet and its orbit. Additional details on each of these steps follow below.

2.1. Radial Velocities

The data sets presented in this work consist of unbinned RV observations taken with seven different instruments: the Levy spectrometer (on the 2.4 m Automated Planet Finder telescope; Vogt et al. 2014), the High Resolution spectrometer (HIRES, on the 10 m Keck I telescope; Vogt et al. 1994), the Planet Finder spectrometer (PFS, on the 6.5 m Magellan Clay telescope; Crane et al. 2006, 2008; Crane et al. 2010), the High Accuracy Radial Velocity Planet Searcher (HARPS, on the ESO 3.6 m telescope; Mayor et al. 2003), the High Accuracy Radial velocity Planet Searcher for the Northern hemisphere (HARPS-N, on the 3.58 m Telescopio Nazionale Galileo; Cosentino et al. 2012), the Spectrographe pour l’Observation des PHénomènes des Intérieurs stellaires et des Exoplanètes (SOPHIE, on the 1.93 m reflector telescope at the Haute-Provence Observatory; Bouchy et al. 2011), and the CARMENES spectrometer (on the 3.5 m telescope at the Calar Alto Observatory; Quirrenbach et al. 2018). Samples of the new HIRES, APF, PFS, and HARPS-TERRA velocities used in our analyses are presented in Appendix B, while the full data sets will be made available as machine-readable tables.

The APF, HIRES, and PFS RV values are all measured by placing a cell of gaseous I_2 in the converging beam of each telescope. This imprints the 5000–6200 Å region of incoming stellar spectra with a dense forest of I_2 lines that act as a wavelength calibrator and provide a proxy for the point-spread function (PSF) of each spectrometer. To ensure a constant I_2 column density over multiple decades, the cells are held at a constant temperature of 50.0 ± 0.1 °C. The instruments have typical spectral resolutions of 90,000, 60,000 and 80,000 for

the APF, HIRES, and PFS, respectively. While only the 5000–6200 Å spectral region is used for measuring RVs, the instruments produce spectra from 3700 to 7700 Å for the APF, 3700–8000 Å for HIRES, and 3900–6700 Å for PFS.

Once the iodine region of the spectrum has been extracted, it is split into 2 Å chunks. Each chunk is analyzed using the spectral synthesis technique described in Butler et al. (1996), which deconvolves the stellar spectrum from the I₂ absorption lines and produces an independent measure of the wavelength, instrument PSF, and Doppler shift. The final Doppler velocity from a given observation is the weighted mean of the velocities of all the individual chunks (~700 for the APF and HIRES, and ~800 for PFS). The final internal uncertainty of each velocity is the standard deviation of all 700 chunk velocities about that mean.

In contrast, HARPS, HARPS-N, and SOPHIE make use of multiple observing fibers, one of which is placed on the stellar target while the other is pointed at a Th-Ar calibration lamp to provide a simultaneous wavelength reference. The two HARPS instruments operate in the same region of wavelength space, from 3800 to 6900 Å, and have the same peak resolving power of ~115,000 (Pepe et al. 2002; Cosentino et al. 2012). SOPHIE covers the same wavelength range as the two HARPS instruments, but has a slightly lower resolution of ~75,000.

The HARPS-TERRA velocities presented here are measured using the approach laid out in Anglada-Escudé & Butler (2012), using data obtained from the HARPS instrument described above. Specifically, the spectra for these observations are downloaded from the ESO archive and then each observation is decomposed into (1) a high-S/N template, (2) the RV shift for that observation, and (3) a multiplicative background set of polynomials to account for flux variations. TERRA first derives approximate RVs measured against an observed spectrum and then improves the template by coadding all observed spectra and recomputing the RVs. The spectra are coadded via a weighted least-squares regression with a cubic B-spline.

For the HARPS-N velocities, the data reduction and spectral extraction were carried out using the Data Reduction Software (DRS v3.7). Once an observation is complete, a 2D spectrum is optimally extracted from the resulting FITS file. The spectrum is cross-correlated with a numerical mask corresponding to the appropriate spectral type (F0, G2, K0, K5, or M4), and the resulting cross-correlation function (CCF) is fit with a Gaussian curve to produce the RV measurement (Baranne et al. 1996; Pepe et al. 2002) and calibrated to determine the RV photon-noise uncertainty σ_{RV} . The SOPHIE RVs are calculated using a similar data-reduction pipeline, which is adapted from the HARPS DRS software.

The CARMENES spectrometer consists of two cross-dispersed echelles and also employs multiple observing fibers in order to obtain simultaneous stellar and wavelength calibration data. The first spans 5200–9600 Å in the visible (VIS) at a resolution of 94,600, while the second covers 9600–17100 Å in the near-infrared (NIR) at a resolution of 80,400 (Quirrenbach et al. 2014). CARMENES makes use of the spectrum RV analyzer (SERVAL) software package to produce RV measurements (Zechmeister et al. 2018). SERVAL is based upon the least-squares fitting approach described above and again computes precision RV measurements using a least-squares matching of each observed spectrum to a high-S/N template derived from the same observations.

2.2. Photometry and Stellar Rotation

To search for evidence of a given star’s stellar rotational period, we have acquired high-precision, long-baseline photometric data of HD 190007, GJ 686, and HD 180617 taken with the T12 0.8 m and T4 0.75 m APTs at Fairborn Observatory in the Stromgren *b* and *y* passbands. The two-color observations have been combined to produce a $\Delta(b + y)/2$ joint-filter time series, which improves measurement precision. Program stars on these telescopes have their observations interlaced with three nearby comparison stars in the sequence: dark, A, B, C, D, A, SKYA, B, SKYB, C, SKYC, D, SKYD, A, B, C, D, where A, B, and C are the comparison stars and D is the program star. Integration times are 20–30 s (depending on stellar brightness) on the 0.75 m APT, where the Stromgren *b* and *y* observations are made sequentially, and 40 s on the 0.80 m APT, where the two bands are measured simultaneously (Henry 1999). The photometric data for each target and the resulting conclusions drawn from the data set are described in each star’s respective section of the paper.

2.3. Bayesian Search and Orbital Fitting

The significance of signals initially identified with SYSTEMIC are assessed by calculating likelihood ratios and Bayes factors based on the Bayesian information criterion (BIC; e.g., Liddle 2007; Feng et al. 2016) and by applying a noise model that accounts for the most important sources of variability in an RV time series (Feng et al. 2016), i.e., Keplerian signals, an unknown amount of white noise, different unknown levels of correlated noise, and potential linear correlations between velocities and available spectroscopic activity proxies. The model has been discussed in great detail in, e.g., Feng et al. (2016, 2017a) and Díaz et al. (2018).

The model for a given star’s RV solution is made up of a combination of signal and noise components, where the signal for N_p planets in the k th RV data set is given by Equation (1):

$$\hat{v}_s^k(t_j) = \sum_{i=1}^{N_p} K_i [\sin(\omega_i + \nu_i(t_j)) + e_i \cos \omega_i] + \gamma_k + \dot{\gamma}_k t_j, \quad (1)$$

where K_i is the RV semi-amplitude of the stellar variation induced by the i th planet’s gravitational pull on the host star, $\nu_i(t_j)$ is the true anomaly derived from the planet’s orbital period p_i , eccentricity e_i , and the reference mean anomaly M_0 after solving Kepler’s equation. Unlike Feng et al. (2019), we do not include a linear trend in the model as in some cases we find evidence of signals with periods approaching the RV data time span. We therefore replace the linear trend by an offset to avoid introducing degeneracies between potential long-period Keplerian signals and a linear trend term in the model.

We assess each RV data set to determine whether it is best represented by a white-noise model (a constant jitter is used to fit excess noise), or a moving average model (MA(1); Tuomi et al. 2013). In order to determine the order, q , of the MA model, we calculate the maximum likelihood for an MA model using the Levenberg–Marquardt (LM) optimization algorithm. We calculate $\ln(\text{BF})$ for MA($q+1$) and MA(q). If $\ln(\text{BF}) < 5$, we select MA(q). If $\ln(\text{BF}) > 5$, we select MA($q+1$) and keep increasing the order of the MA model until the model with the highest order passing the $\ln(\text{BF}) > 5$ criterion is found. Additional details on this model determination process can be found in Feng et al. (2019).

Once the appropriate model has been determined, we search for periodic signals in the data by applying an adaptive Metropolis algorithm by Haario et al. (2006) combined with a parallel tempering scheme designed by Feng et al. (2019). This Markov Chain Monte Carlo technique has been applied to similar data sets (e.g., Butler et al. 2017; Vogt et al. 2017; Tuomi et al. 2018) and found to identify significant signals reliably with a low sensitivity to false positives (Dumusque et al. 2017). A signal is considered to be strong if the logarithmic Bayes factor is larger than 3 (i.e., $\ln(\text{BF}) > 3$) or, equivalently, if its BIC is larger than 6 (Kass & Raftery 1995). A signal is considered to be very strong or significant if $\ln(\text{BF}) > 5$. The exact number of free parameters needed for the RV fit is unknown, however, as a circular Keplerian model has three free parameters while an eccentric Keplerian orbit requires five. We therefore define $k = 3$ and $k = 5$ as the boundaries for the real BIC value, which are represented in the fit summaries as $\ln(\text{BF}_3)$ and $\ln(\text{BF}_5)$, respectively. Because we are using a sinusoidal model in the calculation of the BFPs, we use $\ln(\text{BF}_3) = 5$ as the initial threshold for declaring a signal to be significant. Although a more conservative criterion of $\ln(\text{BF}) > 6.9$ is proposed by Nelson et al. (2020), we keep using $\ln(\text{BF}) > 5$ in order to be consistent with the threshold proposed by Kass & Raftery (1995) and suggested by Feng et al. (2016) through analyses of RV data sets. Nevertheless, the results presented in this work are not sensitive to the choice of $\ln(\text{BF})$ criterion because all planets satisfy the more conservative $\ln(\text{BF}) > 6.9$ criterion. The real significance of a signal, however, is determined through posterior sampling combined with the BF thresholds. This analysis is visualized by creating a $\ln(\text{BF})$ periodogram (BFP) for each of the individual RV data sets, in addition to a BFP for the combined RV data set.

In an attempt to identify those signals caused by stellar activity, we calculate BFPs for the activity indices and the observational window function for each data set and perform visual inspections to determine whether they exhibit overlapping periods with potential planetary signals in the RV data sets. To assess the consistency of signals over time, we compute a moving periodogram for those signals whose phase is well covered by the RV data. Because the RVs are typically not measured in a uniform way, the consistency of a true signal may depend on the sampling cadence even if the power is normalized. However, it is easy to identify false positives if inconsistency is found at high-cadence epochs with a timescale comparable with or longer than the signal period (Feng et al. 2019).

A full set of white noise, moving average, and autoregressive BFPs for each target star’s RV data sets, activity indicators, and window function is presented in Appendix A.

2.4. Stellar Activity Indicators

The derived spectral activity indicators from each of our HIRES, PFS, and APF spectra serve as proxies for chromospheric activity in the visible stellar hemisphere at the moments when the spectra were obtained. The S index is obtained from measurement of the emission reversal at the cores of the Fraunhofer H and K lines of Ca II located at 3968 \AA and 3934 \AA , respectively (Duncan et al. 1991).

For the APF data, we employ an adaptation of the S -index analysis presented in Isaacson & Fischer (2010) where, for each star, we identify the observation with the highest S/N

level as the “reference spectrum” and then compute the redshift of that spectrum by cross-correlating with the NSO solar atlas. All other spectra are then shifted into the same reference frame and continuum aligned to that reference spectrum using 10 \AA continuum regions in order to remove flux differentials arising from different S/Ns between the exposures. The flux in the Ca II H & K bands and their associated continuum bands are measured and recorded, and the final data sets are calibrated against the original Mt. Wilson S -index survey results to allow for comparisons with our Keck and PFS data.

We also report H -index measurements for our APF, PFS, and postfix (taken after the detector upgrade in 2004 August) HIRES spectra. Similarly to the S index, the H index quantifies the amount of flux within the $H\alpha$ Balmer line core compared to the local continuum. Details on the prescription used for the HIRES and PFS data sets can be found in Butler et al. (2017). For the APF, we use the Gomes da Silva et al. (2011) prescription, which defines the H index as the ratio of the flux within $\pm 0.8 \text{ \AA}$ of the $H\alpha$ line at 6562.808 \AA to the combined flux of two broader flanking wavelength regions: $6550.87 \pm 5.375 \text{ \AA}$ and $6580.31 \pm 4.375 \text{ \AA}$. The H -index measurements often show peaks at periods of roughly one year due to the presence of shallow telluric lines that can shift into and out of the $H\alpha$ filter if the star’s systemic RV places them on the edge of the $H\alpha$ line. We find that attempts to remove these lines change the shape and flux level of the $H\alpha$ line in substantial ways that compromise the search for flux modulations indicative of stellar activity. Therefore, we do not remove the tellurics, but rather search for additional signals in the H -index periodograms after removing the one-year cycles.

For the HARPS data sets, which we process through the HARPS-TERRA pipeline, we also make use of the Ca II H & K activity indicators that TERRA measures, in addition to the line bisectors (BIS), FWHM, and CCF, which are taken from the original HARPS DRS results.

We analyze the resulting activity indicators by computing Bayes factor periodograms for each activity indicator in each RV data set and looking for any well-defined peaks with $\ln(\text{BF}_3) > 5$ at or near the period of our suspected planets. In cases where we see peaks in these regions, we then compute the correlation coefficients between the RV measurements and the activity indicator measurements to look for evidence that the stellar activity is influencing the star’s RVs.

3. Stellar Parameters

All four stellar hosts described herein are nearby dwarf stars with spectral types from K0V to M3V. These stars make excellent candidates for traditional iodine-cell-based RV spectrometers thanks to their relatively bright V magnitudes and abundance of narrow absorption lines in the visible part of the spectrum (Burt et al. 2015). These stars in particular were selected for inclusion in the long-running Lick–Carnegie Exoplanet Survey (LCES) carried out in B17 using Keck HIRES after analysis of early spectra revealed them to be chromospherically inactive and slowly rotating—two other key characteristics for RV candidates. Two of the stars (HD 190007 and HD 216520) do not have previously known exoplanets, which often prompts in-depth study of stellar characteristics. Their proximity to Earth and resulting bright magnitudes, however, have led to their inclusion in a number of different surveys and large stellar characterization efforts (see, e.g., Lépine & Gaidos 2011; Mann et al. 2015; Brewer et al. 2016)

Table 1
Stellar Parameters

Parameter	HD 190007	HD 216520	GJ 686	HD 180617
R.A.	20 02 47.05 (a)	22 47 31.88 (a)	17 37 53.35 (a)	19 16 55.26 (a)
Decl.	03 19 34.27 (a)	83 41 49.30 (a)	18 35 30.16 (a)	05 10 08.04 (a)
Spectral type	K4V(k) (b)	K0V (c)	M1.0V (d)	M2.5V (d)
ϖ (mas)	78.6238 ± 0.0617 (a)	51.1167 ± 0.0292 (a)	122.5609 ± 0.0346 (a)	169.1590 ± 0.0520 (a)
Distance (pc)	12.72 ± 0.01 (a)	19.56 ± 0.011 (a)	8.159 ± 0.0023 (a)	5.912 ± 0.0018 (a)
Systemic RV (km s ⁻¹)	-30.467 ± 0.133 (a)	-18.536 ± 0.182 (a)	-10.092 ± 0.232 (a)	35.554 ± 0.158 (a)
V	7.46 (e)	7.53 (e)	9.62 (e)	9.12 (e)
G	7.0634 (a)	7.2790 (a)	8.7390 (a)	8.0976 (a)
M_V	6.94 ± 0.01 (a), (e)	6.08 ± 0.02 (a), (e)	10.04 ± 0.03 (a), (e)	10.26 ± 0.005 (a), (e)
M_G	6.54 (a), (e)	5.82 (a), (e)	9.18 (a), (e)	9.24 (a), (e)
$B - V$	1.128 ± 0.015 (e)	0.867 ± 0.010 (e)	1.530 ± 0.015 (e)	1.464 ± 0.005 (e)
$B_p - R_p$	1.3534 (a)	1.0496 (a)	2.1173 (a)	2.3816 (a)
K_s	4.796 ± 0.017 (f)	5.449 ± 0.021 (f)	5.572 ± 0.020 (g)	4.673 ± 0.020 (g)
Mass (M_\odot)	0.77 ± 0.02 (tw)	0.82 ± 0.04 (tw)	0.426 ± 0.017 (d)	0.484 ± 0.019 (d)
Radius (R_\odot)	0.79 ± 0.039 (h)	0.760 ± 0.007 (tw)	0.427 ± 0.013 (d)	0.481 ± 0.014 (d)
log luminosity (L/L_\odot)	-0.68 ± 0.01 (i)	-0.452 ± 0.004 (tw)	-1.53 ± 0.011 (d)	-1.49 ± 0.0052 (d)
[Fe/H]	0.16 ± 0.05 (j)	-0.16 (g)	-0.23 ± 0.16 (d)	-0.04 ± 0.16 (d)
T_{eff} (K)	4610 ± 20 (tw)	5103 ± 20 (tw)	3656 ± 51 (d)	3534 ± 51 (d)
log(g) (cm s ⁻²)	4.58 ± 0.02 (k)	4.54 ± 0.028 (g)	4.87 ± 0.07 (d)	4.90 ± 0.07 (d)
P_{rot} (days)	28.626 ± 0.046 (tw)	unknown	38.732 ± 0.286 (tw)	50.60 ± 0.41 (tw)
$v \sin i$ (km s ⁻¹)	2.55 (l)	0.2 ± 0.5 (g)	2.49 (m)	<2 (n)
RV data	APF, HIRES	APF, HIRES	APF, HIRES, PFS HARPS, HARPS-N SOPHIE, CARMENES	APF, HARPS HIRES CARMENES

Note. (a) Gaia Collaboration et al. (2018). (b) Gray et al. (2006). (c) Gray et al. (2003). (d) Schweitzer et al. (2019). (e) ESA (1997). (f) Cutri et al. (2003). (g) Brewer et al. (2016). (h) Kervella et al. (2019). (i) Biazzo et al. (2007). (j) Mishenina et al. (2013). (k) Franchini et al. (2014). (l) Mishenina et al. (2012). (m) Houdebine et al. (2016). (n) Reiners et al. (2018). (tw) this work.

that provide us with the parameters for each star presented in Table 1. The stars have also been examined by Mishenina et al. (2013), which provides individual elemental abundances (Table 2). For the other two targets with previously published planets (GJ 686 and HD 180617), we take the stellar parameters from Schweitzer et al. (2019).

4. HD 190007

HD 190007 (GJ 775, HIP 98698) is a nearby (12.714 ± 0.010 pc),¹⁷ relatively bright ($V = 7.46$; ESA 1997), K4V(k) star (Gray et al. 2006; see summary of parameters in Table 1) The star is a moderately active star showing elevated chromospheric emission via Ca H & K ($\log R'_{\text{HK}} = -4.652$; Olsperg et al. 2018) and coronal X-ray emission ($\log L_X/L_{\text{bol}} = -4.98$; Hinkel et al. 2017). HD 190007 was classified as a BY Dra variable and designated V1654 Aql in the General Catalogue of Variable Stars (GCVS) by Kazarovets et al. (2003) based on the observed photometric variability reported by Lockwood et al. (1997; b -band amplitude of 0.016 mag). BY Draconis variables are usually K- or M-type dwarfs that display quasiperiodic photometric variations on timescales of hours to months with amplitudes from 1 to 500 mmag that are believed to be driven by surface spots and chromospheric activity (e.g., López-Morales et al. 2006). While the eponymous star BY Dra itself is a close binary ($P = 6$ days) and many BY Dra stars are close binaries, the manifestations of magnetic activity (starspots, strong emission lines) are tied to relatively rapid rotation (Bopp & Espenak 1977). The star's

¹⁷ $\varpi = 78.6238 \pm 0.0617$ mas (Gaia Collaboration et al. 2018) and distance calculated as $1/\varpi$, including parallax zero-point shift from Lindegren et al. (2018).

Table 2
Stellar Abundances from Mishenina et al. (2013)

Species	HD 190007	HD 216520
[Fe/H]	0.16	-0.17
[O/Fe]	-0.16	0.20
[Mg/Fe]	-0.11	0.09
[Si/Fe]	0.10	0.01
[Ca/Fe]	0.13	0.02
[Ni/Fe]	0.03	-0.07
[Y/Fe]	-0.06	-0.13
[Zr/Fe]	-0.19	0.00
[Ba/Fe]	-0.03	-0.20
[La/Fe]	-0.18	-0.12
[Ce/Fe]	-0.20	0.00
[Nd/Fe]	-0.16	0.07
[Sm/Fe]	-0.15	0.08
[Eu/Fe]	-0.04	0.09

Note. Based on the discussion in Mishenina et al. (2008, 2013), the abundance uncertainties are on the order of ± 0.06 dex for Fe, Mg, and Si, ± 0.1 dex for O, Ca, and Ni, and ± 0.1 – 0.15 dex for Y, Zr, Ba, La, Ce, Nd, Sm, and Eu.

level of chromospheric and coronal activity, and observed amplitude of photometric variability (e.g., Radick et al. 1998; Mamajek & Hillenbrand 2008), appears to be normal for a mid-K dwarf with its rotation period of $P_{\text{rot}} = 28.626 \pm 0.046$ days (Table 1, Section 4.3). The published T_{eff} estimates mostly cluster between ~ 4500 K and 4700 K (see Table 3), and we adopt $T_{\text{eff}} = 4610 \pm 20$ K.

Previous analyses of the star show good agreement on HD 190007 being slightly metal rich (e.g., [Fe/H] = 0.14 \pm 0.06, Ramírez et al. 2012; 0.16 \pm 0.05, Mishenina et al. 2013),

Table 3
 T_{eff} and M_* Estimates for HD 190007

T_{eff} (K)	Reference
4352 ± 70	Houdebine (2012)
4466	Katz et al. (2011)
4541 ⁺⁸⁰ ₋₄₃	Boeche & Grebel (2016)
4568 ± 23	Houdebine et al. (2019)
4571 ± 117	Bai et al. (2019)
4596 ± 40	Luck (2017)
4597 ± 8	Franchini et al. (2014)
4599 ± 85	Ramírez et al. (2012)
4603 ± 91	Aguilera-Gómez et al. (2018)
4611 ± 40	González Hernández & Bonifacio (2009)
4616 ± 10	Stevens et al. (2017)
4637 ± 51	Casagrande et al. (2006)
4640 ± 51	Casagrande et al. (2010)
4650	Luck & Heiter (2005)
4681 ± 1	Biazzo et al. (2007)
4709	Anders et al. (2019)
4722	Stassun et al. (2018)
4724 ± 7	Mishenina et al. (2008)
4724	Frasca et al. (2015)
4610 ± 20	adopted T_{eff}
M_* (M_{\odot})	Reference
0.80	Wright et al. (2011)
0.785 (0.773–0.801)	Takeda et al. (2007)
0.778 ± 0.039	Kervella et al. (2019)
0.774	a
0.772	b
0.76	Luck (2017)
0.760 ± 0.091	Stassun et al. (2018)
0.752 ± 0.043	c
0.751 (0.732–0.801)	Anders et al. (2019)
0.73 ^{+0.03} _{-0.01}	Ramírez et al. (2012)
0.77 ± 0.02	adopted M_*

Note. (a) From Chen et al. (2014) isochrone matching Hyades ([Fe/H] = 0.18, $Z = 0.0193$, $\log(\text{age}/\text{yr}) = 8.85$), following Torres (2019). (b) Using the luminosity–mass calibration from Eker et al. (2018). (c) From the fit of M_V to the mass for FGK dwarfs for detached binary stars compiled by Torres (2010).

similar to the well-studied Hyades cluster (Fe/H \simeq 0.15–0.18, Dutra-Ferreira et al. 2016; Liu et al. 2016; Cummings et al. 2017). This metallicity enhancement likely explains why the star is slightly above the main sequence in $B - V$ versus M_V space ($dM_V \sim -0.16$; Isaacson & Fischer 2010). An upper limit on the ages of thin-disk stars this metal-rich is roughly < 8 Gyr (Mishenina et al. 2013).

The star has multiple published mass estimates, compiled in Table 3; however, we complement these values with some new independent estimates based on the luminosity and absolute magnitude. The star has metallicity similar to the Hyades cluster, which has [Fe/H] \simeq +0.18 (Dutra-Ferreira et al. 2016), and an age of $\sim 700 \pm 100$ Myr (Brandt & Huang 2015; Gossage et al. 2018; Martín et al. 2018; Lodieu et al. 2019). Torres (2019) has found that stars in eclipsing binaries in the Hyades show reasonable agreement in their mass versus absolute magnitude trend against the PARSEC evolutionary tracks (Chen et al. 2014) for [Fe/H] = +0.18 and 625–800 Myr isochrones. Using the Chen et al. (2014) isochrone matched to the Hyades, the absolute magnitude ($M_V = 6.94$) corresponds to mass $0.774 M_{\odot}$. K dwarfs evolve very slowly,

and indeed, a 5 Gyr isochrone for the same chemical composition yields mass $0.756 M_{\odot}$ for the same M_V . Using the mass–luminosity trend for main-sequence stars from Eker et al. (2018) yields a mass estimate of $0.772 M_{\odot}$. If one fits a quadratic¹⁸ to the absolute magnitudes versus $\log(\text{mass})$ for the well-characterized FGK dwarf detached binaries compiled in the review by Torres (2010), for $M_V = 6.94$, one would predict $0.752 \pm 0.043 M_{\odot}$. The distribution of mass estimates is tightly clustered in Table 3, and we simply adopt $M_* = 0.77 \pm 0.02 M_{\odot}$ based on the mean and standard deviation (representing the scatter among multiple methods to derive the mass).

Multiple independent age estimates can be made using the star’s rotation and activity indicators. Using the X-ray age calibrations from Mamajek & Hillenbrand (2008), we estimate an X-ray age estimate of 0.9 Gyr, which is in general agreement with previously published ages from X-rays (1.08 Gyr, Vican 2012), rotational age-dating (1.5 ± 0.3 Gyr and 2.0 ± 0.4 Gyr from Ramírez et al. 2012; Aguilera-Gómez et al. 2018, respectively), and high-resolution visible spectra (0.88 Gyr, Kóspál et al. 2009). However, recent results from Kepler and K2 studies of young clusters show that the rotational evolution of K dwarfs shows significant stalling between ages of ~ 0.7 and 1 Gyr, and that a Skumanich-like rotational evolution law is a poor approximation (Curtis et al. 2019). Comparing the star’s combination of color ($B_p - R_p = 1.3534$, Gaia Collaboration et al. 2018) or T_{eff} , and rotation period to young clusters and field dwarfs in the Kepler field (Curtis et al. 2019), we find that the star is clearly older than 1 Gyr, and its age is likely typical for field stars in the Kepler field.

Variations in published RVs show evidence of a linear trend on the order of 0.5 km s^{-1} over ~ 16 yr that could be due to a stellar or substellar companion (Soubiran et al. 2013). HD 190007 does not, however, show evidence of a significant tangential velocity anomaly ($dV_t = 13.89 \pm 8.16 \text{ m s}^{-1}$) nor an abnormally high Gaia DR2 RUWE value (RUWE = 0.89), either of which would lend additional support to the possibility of a binary companion (Gaia Collaboration et al. 2016; Kervella et al. 2019). HD 190007 has not previously been the target of high-resolution imaging efforts to look for stellar companions using the VLT (NACO or SPHERE) or Gemini (using GPI, NIRI, or NICI), nor has it been targeted by Robo-AO. Such observations may help clarify the trend seen in the previously published RV data, and we encourage such follow-up efforts.

Based on its Gaia DR2 results, we find that HD 190007 has a barycentric galactic velocity of $U = -22.097 \pm 0.006 \text{ km s}^{-1}$, $V = -16.461 \pm 0.006 \text{ km s}^{-1}$, $W = 15.442 \pm 0.007 \text{ km s}^{-1}$ with U measured toward the Galactic center, V in the direction of Galactic rotation, and W toward the North Galactic Pole (ESA 1997). Adopting the local standard of rest (LSR) from Bland-Hawthorn & Gerhard (2016) gives $U_{\text{LSR}} = -12.1 \text{ km s}^{-1}$, $V_{\text{LSR}} = -5.5$ and $W_{\text{LSR}} = 22.4 \text{ km s}^{-1}$, for a total LSR velocity of 26.1 km s^{-1} . Following the kinematic selection criteria of Bensby et al. (2014), we estimate kinematic membership probabilities of $P_{\text{thin}} = 98.74\%$, $P_{\text{thick}} = 1.26\%$, $P_{\text{halo}} = 0.0003\%$, and the probability of membership in the Hercules dynamical stream as $P_{\text{Hercules}} = 0.00007\%$. Mackereth & Bovy (2018) calculate that

¹⁸ $\log_{10}(M/M_{\odot}) = 0.4391 - 0.107645 M_V + 3.818613e - 3 M_V^2$. The fit is appropriate for FGK dwarfs (although anchored to late A’s and early M’s) over $1.6 < M_V < 9.0$. The rms scatter is about 5.7% and likely dominated by the differences in chemical abundances and ages among the field dwarfs in the Torres (2010) review.

HD 190007’s Galactic orbit has 3D pericenter and apocenter radii of 6.998 and 8.103 kpc, respectively, an eccentricity of 0.07306, and a maximum vertical excursion of 0.336 kpc. The star’s *Banyan Σ* , a Bayesian classification tool that identifies members of young moving groups, yields $P_{\text{field}} = 99.9\%$ independent of whether the star’s default RV or Gaia DR2 RV is used, so it does not appear to belong to any known nearby young moving groups (Gagné et al. 2018).

We use the measured abundances for the α elements Mg, Si, and Ca, and the Fe abundance from Mishenina et al. (2013) to estimate the α enrichment $[\alpha/\text{Fe}]$ (e.g., Bovy 2016). Adopting unweighted means of the abundances of three α elements with respect to iron, we estimate $[\alpha/\text{Fe}] \simeq 0.04$. Similarly, Franchini et al. (2014) estimate $[\alpha/\text{Fe}] = 0.03 \pm 0.01$. These kinematic calculations and abundance ratios suggest that the star is a metal-rich thin-disk star (e.g., Mishenina et al. 2013).

HD 190007 will not be surveyed during the primary mission of NASA’s TESS satellite, which would have allowed for more detailed characterization of the star’s brightness modulations, due to its proximity to the Earth and Moon contamination zone that the TESS observing plan has been shifted to avoid.

4.1. HD 190007 Radial Velocities

The RV data set for HD 190007 contains observations from two instruments, HIRES on Keck I and the APF’s Levy spectrometer. The Keck data comprise 34 unbinned velocities (32 individual epochs) obtained from 1998 June to 2014 September with a mean internal uncertainty of 1.54 m s^{-1} . The APF data comprise 157 unbinned velocities (91 individual epochs) obtained from 2013 July to 2019 October with a mean internal uncertainty of 1.50 m s^{-1} . Analysis of the combined data set reveals a prominent peak at 11.72 days (Figure 1).

To discern whether this signal could be caused by nonplanetary sources, we first examine the spectral window function of the combined data set (Figure 1). Notable peaks in the window function—such as the peak at $P = 1.0$ days that results from nighttime observing restrictions—can cause aliases to appear at $f_{\text{alias}} = f_{\text{planet}} + f_{\text{WF}}$ (Dawson & Fabrycky 2010). None of the periods that we would expect from this star’s combined window function show up prominently in the 11–12 day range of the RV periodogram, and thus we do not suspect observational aliases of masquerading as the 11.72 day signal.

4.2. HD 190007 Activity Indicators

Only seven observations of HD 190007 were taken with Keck HIRES after the detector upgrade that expanded HIRES’ wavelength range and enabled measurement of the $H\alpha$ line, which is not a large-enough data set to compute a meaningful Bayes factor periodogram. None of the periodograms of the three available activity data sets (S and H indices from the APF, and S index from HIRES) show peaks at or near the proposed 11.72 day planet period (Figure 2). Based on the lack of notable signals at periods matching our potential planet signal, we conclude that the 11.72 day signal is not due to the varieties of stellar activity that produce variance in the emission of the Ca II H&K and $H\alpha$ spectral features.

The APF S - and H -index measurements show evidence of a relatively broad signal with period, $P \sim 29.18$ days, which we take to be a sign of rotational modulation due to its close match with the stellar rotation period as identified in Section 4.3.

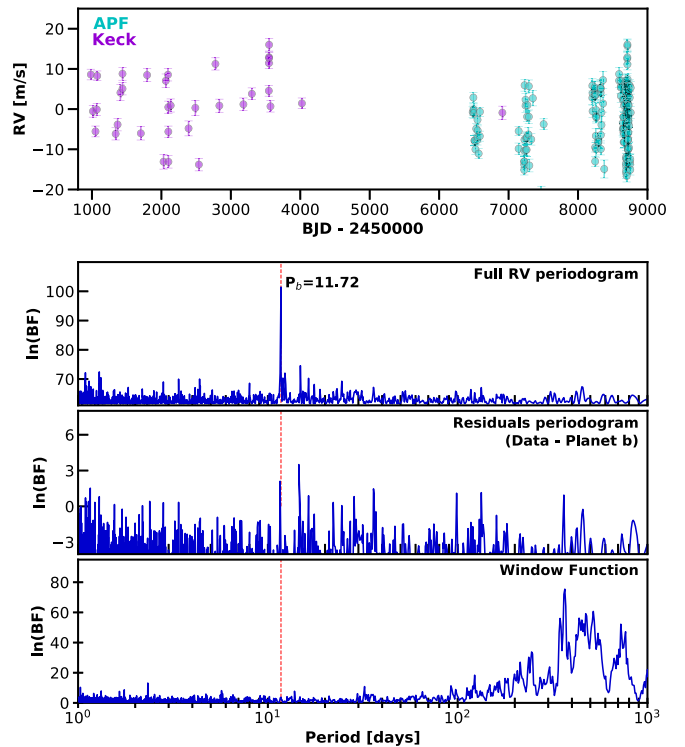


Figure 1. First panel: unbinned RV measurements of HD 190007 taken with the APF (cyan) and Keck HIRES (purple). Second panel: Bayes factor periodogram of the RV data showing the potential planet peak at 11.72 days. Third panel: Bayes factor periodogram of the RV residuals after the 11.72 day signal has been modeled and removed. Fourth panel: spectral window function of the combined RV data sets.

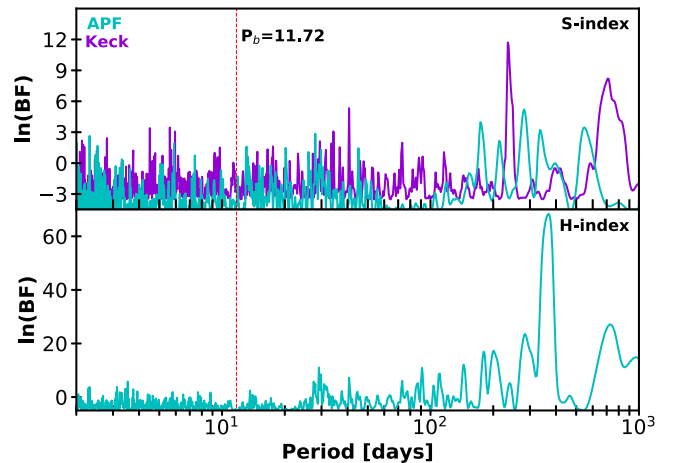


Figure 2. Top: Bayes factor periodogram of the S -index values measured from the APF and Keck HIRES data sets in cyan and purple, respectively. Bottom: same as above, but for the H -index measurements extracted from the APF data. In both panels, there are no prominent peaks in the vicinity of the proposed planet period of 11.72 days, but there is a broad activity-based peak at 29.18 days that is likely tied to rotational modulation evident in the APF activity indicators. The Keck HIRES data set contains only six observations able to produce H -index measurements, which is insufficient to produce an informative periodogram.

Fitting a Keplerian model to this long-term signal produces a best-fit period of $P = 29.180 \pm 0.012$ days and an RV semiamplitude of $K = 3.54 \pm 0.90 \text{ m s}^{-1}$ (Figure 3). While we believe the signal to be due to stellar variability and not an additional planet, as the signal does not appear with significant

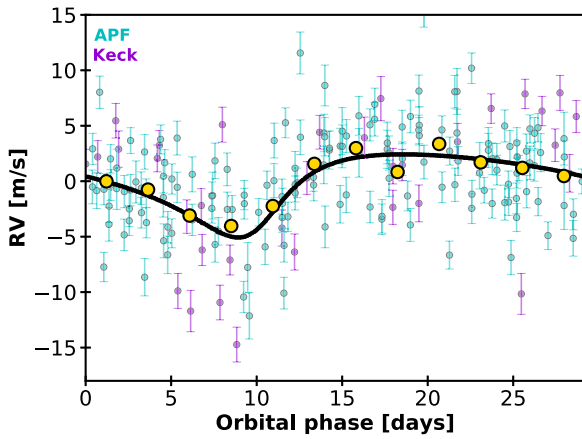


Figure 3. RV observations of HD 190007 phase-folded to the best-fit period of the suspected rotational activity cycle, $P_{\text{act}} = 29.18$ days, with APF observations shown in cyan and Keck HIRES observations shown in purple. The error bars include the excess white-noise “jitter” from our analysis, and the black solid curve denotes the maximum a posteriori Keplerian model. Yellow points depict the phase-binned RV data. Yellow points depict the phase-binned RV data.

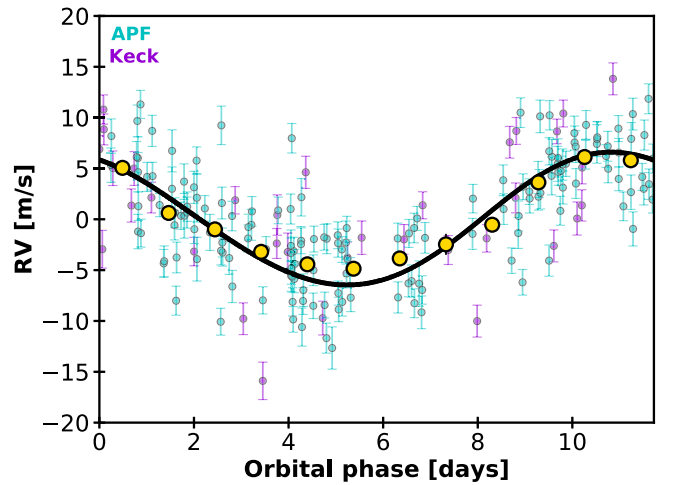


Figure 5. RV observations of HD 190007 phase-folded to the best-fit period of $P = 11.72$ days, with APF observations in cyan and Keck HIRES observations in purple. The error bars include the excess white-noise “jitter” from our analysis, and the black solid curve denotes the maximum a posteriori Keplerian model. Yellow points depict the phase-binned RV data.

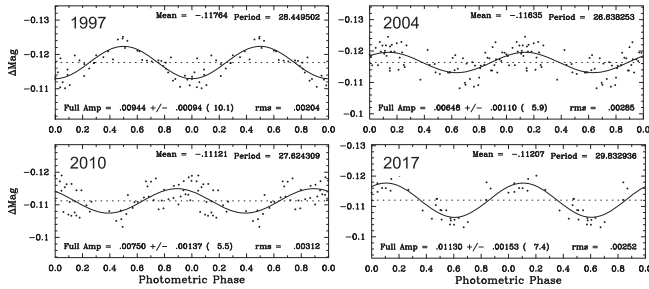


Figure 4. A selection of 4 of the 19 seasons of photometry in which HD 190007 displayed a significant rotation signal. Analyzing the combined set of 19 seasons of rotational periods, we derive a weighted-mean rotation period of 28.626 ± 0.046 days, which is in general agreement with the 29.18 day activity signal measured using the APF S - and H -index activity indicators.

power in the combined RV periodogram, we still included the signal in our overall RV model of the system.

4.3. HD 190007 Photometry and Stellar Rotation

A total of 1092 observations were obtained over 21 observing seasons, spanning 1997 through 2017 using the T4 0.75 m APT at Fairborn Observatory. The comparison stars used in the data analysis are HD 190521, (a K0III star with $V = 7.60$, $B - V = 1.15$) and HD 187406 (an F3V star with $V = 7.67$, $B - V = 0.48$). The photometry shows that HD 190007 varies from year to year by roughly ~ 0.016 mag. When searching the data for rotation periods, we find significant signals in all seasons except those covering 1999 and 2001. The star does, however, appear to be “double spotted” in the years 2000, 2002, 2006, and 2015. In these cases, the rotation period is twice the observed photometric period. Analyzing the 19 seasons where we measure rotational periods, we derive a weighted-mean rotation period of 28.626 ± 0.046 days (Figure 4), which is well separated from the proposed planet periods of 11.72 days but overlaps closely with the ~ 29 day signal seen in the APF activity indicators. This rotation period is also in agreement with the $P_{\text{rot}} = 27.68 \pm 0.36$ days derived in Olsper et al. (2018).

4.4. HD 190007 Orbital Parameters

Having concluded that neither our observing scheme, the star’s chromospheric activity, nor the star’s rotation could be causing the 11.72 day signal we observe in HD 190007’s RV periodogram, we move on to testing whether or not the RV data provide enough Bayesian evidence to support the existence of the suspected planet. We apply a statistical model accounting for Keplerian signals and red noise, as well as correlations between RVs and activity data (see Section 2).

The resulting fit to the data reveals a planet with a period of 11.72 days, a semi-amplitude of $K = 5.64 \text{ m s}^{-1}$, and an eccentricity of $e = 0.14$ (Figure 5, Table 5). This corresponds to a $16.46 M_{\oplus}$ planet orbiting 0.092 au from its host star. The signal is detected at $\ln(\text{BF}_5) = 29.2$, well above the $\ln(\text{BF}_5) = 5$ limit we set for identifying a signal as statistically significant. Thus, we promote the 11.72 day signal to being labeled as a newly identified planet candidate, HD 190007 b.

5. HD 216520

HD 216520 (HIP 112527) is a $V = 7.53$, K0V star (Gray et al. 2003) located 19.6 parsecs away in the constellation of Cepheus ($\varpi = 51.1167 \pm 0.0292$ mas; Gaia Collaboration et al. 2018). The metallicity of the star has been estimated in several studies, with values ranging between $[\text{Fe}/\text{H}] = -0.22$ and -0.14 , with median value $[\text{Fe}/\text{H}] = -0.17$, i.e., slightly metal poor (Mishenina et al. 2008, 2012; Brewer et al. 2016; Luck 2017; Mikolaitis et al. 2019). Effective temperature and mass estimates for HD 216520 are shown in Table 4. We adopt the recent T_{eff} value from Luck (2017), whose value (5130 ± 20 K) falls near the middle of a tight cluster of recent estimates from high-resolution spectroscopy surveys including Mishenina et al. (2008), Bermejo et al. (2013), Brewer et al. (2016), Luck (2017), and Mikolaitis et al. (2019).

We calculate the bolometric luminosity using the Virtual Observatory SED Analyzer (VOSA)¹⁹ from Bayo et al. (2008). We use VOSA to query archival UV/Vis/IR photometry from several sources (Galaxy Evolution Explorer,

¹⁹ <http://svo2.cab.inta-csic.es/theory/main/>

Table 4
 T_{eff} and M_* Estimates for HD 216520

T_{eff} (K)	Reference
5082 ± 25	Brewer et al. (2016)
5103 ± 20	Luck (2017)
5119 ± 7.3	Mishenina et al. (2008)
5119 ± 50	Mikolaitis et al. (2019)
5140^{+59}_{-27}	Gaia Collaboration et al. (2018)
5156 ± 132	Bai et al. (2019)
5163 ± 72	Bermejo et al. (2013)
5103 ± 20	adopted T_{eff}
M_* (M_{\odot})	Reference
0.78	a
0.79 ± 0.02	Brewer et al. (2016)
0.808 ± 0.040	Kervella et al. (2019)
0.84	b
0.84 ± 0.02	Luck (2017)
0.844 ± 0.049	b
0.850 ± 0.103	Stassun (2019)
0.900 ± 0.045	Kervella et al. (2019)
0.82 ± 0.04	adopted M_*

Note. (a) Using the Chen et al. (2014) isochrone for $[M/H] = -0.16$ for age 6 Gyr. (b) Using the Eker et al. (2018) mass–luminosity trend for adopted luminosity. (c) From the fit of M_V to mass for FGK dwarfs for detached binary stars compiled by Torres (2010).

GALEX; Tycho; Gaia DR2; 2MASS; Wide-field Infrared Survey Explorer, WISE)²⁰ and fit synthetic stellar spectra in order to constrain the star’s bolometric flux and independently check the T_{eff} estimates. We find a best-fit BT-Settl-CIFIST model (constraining $\log(g) = 4.5$ and solar metallicity) with 5100 K, which has bolometric flux $f_{\text{bol}} = 2.949 \times 10^{-8} (\pm 1\%) \text{ erg cm}^{-2} \text{ s}^{-1}$ ($m_{\text{bol}} = 7.33 \pm 0.01$ on the IAU 2015 bolometric scale). Combined with the Gaia DR2 parallax, we estimate the absolute bolometric magnitude to be $M_{\text{bol}} = 5.87 \pm 0.01$, and the luminosity to be $\log(L/L_{\odot}) = -0.452 \pm 0.004$. Combining this luminosity estimate with our adopted T_{eff} value yields an estimated radius of $0.760 \pm 0.007 R_{\odot}$. This is similar to recent estimates by Brewer et al. (2016; $0.79 \pm 0.02 R_{\odot}$), Stassun et al. (2019; $0.794 \pm 0.043 R_{\odot}$), and Gaia Collaboration et al. (2018; $0.77^{+0.01}_{-0.02} R_{\odot}$). All of these radii estimates are systematically smaller than those predicted in the JMMC Stellar Diameter Catalog (JSDC; Version 2; Chelli et al. 2016; Bourges et al. 2017), which estimates an angular diameter of $\theta_{\text{LD}} = 0.3989 \pm 0.0093 \text{ mas}$ (and when combined with the Gaia DR2 parallax yields an radii estimate of $0.839 \pm 0.020 R_{\odot}$). In Table 4, we list several published mass estimates and three new independent ones based on the the estimates of the star’s luminosity and absolute magnitude. We adopt a mass of $0.82 \pm 0.04 M_{\odot}$ for HD 216520, which spans the range of masses estimated using evolutionary tracks and empirical trends.

Measurements of the star’s chromospheric activity through the Ca H & K S index and $\log R'_{\text{HK}}$ indices show the star to be relatively inactive, indeed similar to that of the Sun. Isaacson & Fischer (2010) report 124 epochs of Ca H & K measurements,

showing the star’s activity ranging from $\log R'_{\text{HK}} = -4.860$ to -5.006 . These values span a range not too much wider than that observed over typical solar cycles (indeed almost identical to that seen over solar cycle 19; Egeland et al. 2017). Using the rotation–activity–age relations from Mamajek & Hillenbrand (2008), the mean $\log R'_{\text{HK}}$ value from Brewer et al. (2016; -4.93) is consistent with the star’s Rossby number being 2.02, with a predicted rotation period of 43 days and an age of ~ 6.7 Gyr. Previous estimates based on chromospheric activity by Wright et al. (2004) and Isaacson & Fischer (2010) similarly estimated ages and predicted rotation periods of 5.25 Gyr/44.0 days and 5.19 Gyr/42 days, respectively. Isochronal age estimates incorporating the star’s H-R diagram constraints and metallicity and using several different sets of evolutionary tracks by Luck (2017) spanned 4.84 ± 2.81 Gyr.

Based on its Gaia DR2 results, we find that HD 216520 has a heliocentric velocity of $U = 17.458 \pm 0.007 \text{ km s}^{-1}$, $V = -16.905 \pm 0.006 \text{ km s}^{-1}$, and $W = 8.341 \pm 0.009 \text{ km s}^{-1}$ with U measured toward the Galactic center, V in the direction of Galactic rotation, and W toward the North Galactic Pole (ESA 1997). With respect to the LSR of Bland-Hawthorn & Gerhard (2016), the velocities are $U_{\text{LSR}} = +27.5 \text{ km s}^{-1}$, $V_{\text{LSR}} = -5.9 \text{ km s}^{-1}$, and $W_{\text{LSR}} = +15.3 \text{ km s}^{-1}$, with overall LSR velocity of 32.0 km s^{-1} . Using the kinematic criteria of Bensby et al. (2014), we estimate kinematic membership probabilities for HD 216520 for the thin disk, thick disk, halo, and Hercules dynamical stream of $P_{\text{thin}} = 99.005\%$, $P_{\text{thick}} = 1.004\%$, $P_{\text{halo}} = 0.0002\%$, and $P_{\text{Hercules}} = 0.000007\%$. Mackereth & Bovy (2018) calculate that HD 216520’s Galactic orbit has 3D pericenter and apocenter radii of 6.753 and 8.431 kpc, respectively, an eccentricity of 0.11, and a maximum vertical excursion of 0.224 kpc. Chemically and kinematically, the star is squarely consistent with being a member of the thin disk, corroborating previous classifications by Mishenina et al. (2013) and Hinkel et al. (2017). The star’s lithium abundance, $\log A(\text{Li}) = -0.30$ (Mishenina et al. 2012), sets a lower age limit of roughly 0.5 Gyr. Note that the combination of chromospheric activity and metallicity/kinematic constraints shows that the isochronal age of 11.1 Gyr as listed by Brewer et al. (2016, 6.9–13.8 Gyr) seems unlikely. Based on the available constraints from chromospheric activity measurements, isochronal age estimates, and Galactic kinematic constraints, we adopt an age of 6 ± 3 Gyr.

5.1. Radial Velocities

The RV data set for HD 216520 contains observations from two instruments, Keck HIRES and the APF’s Levy spectrometer. The Keck data comprise 504 unbinned velocities (210 individual epochs) obtained from 2001 October to 2017 June with a mean internal uncertainty of 1.26 m s^{-1} . The APF data comprise 300 unbinned velocities (91 individual epochs) obtained from 2014 October to 2020 June with a mean internal uncertainty of 2.02 m s^{-1} .

Combining these data sets, we find two strong, well-defined peaks in the RV periodogram at periods of $P = 35.45$ and 154.43 days. When comparing this period with the data sets’ combined spectral window function, we find no corresponding alias peaks (Figure 6).

²⁰ GALEX: Bianchi et al. (2017), Tycho: ESA (1997), 2MASS: Cutri et al. (2003), WISE: Cutri et al. (2012). Gaia DR2 photometry was omitted as it led to large uncertainty (0.2) in the derived bolometric magnitude.

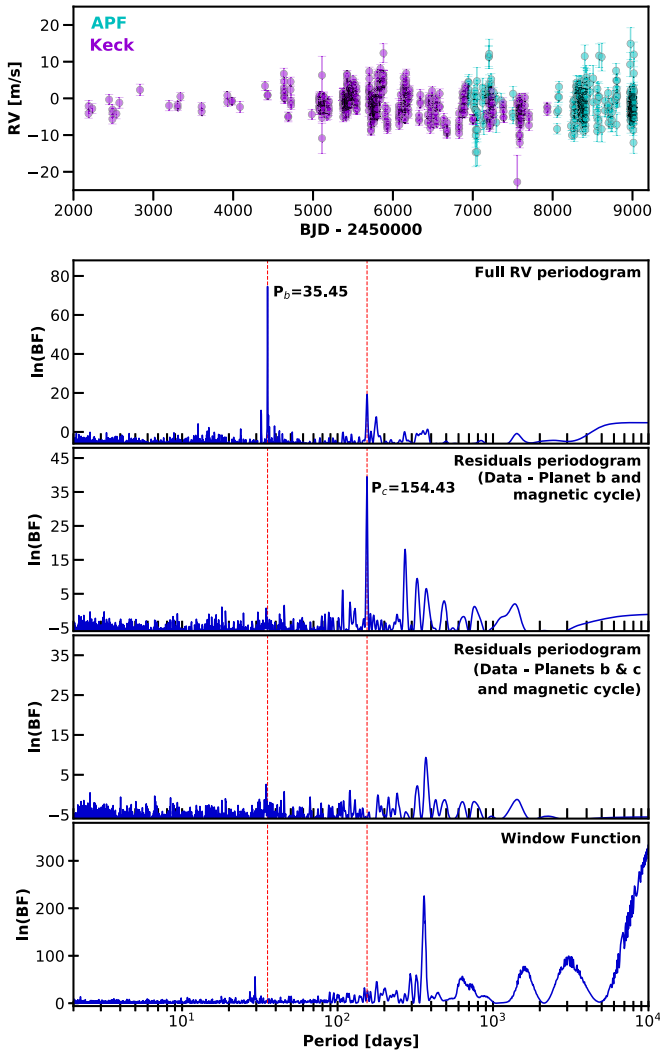


Figure 6. First panel: unbinned RV measurements of HD 216520 taken with the APF (cyan), and Keck HIRES (purple). Second panel: Bayes factor periodogram of the RV data showing the suspected planet peak at 35.45 days. Third panel: Bayes factor periodogram of the RV residuals after the 35.45 day Keplerian signal and the ~ 7700 activity signal have been fit and removed from the data sets. The second suspected planet peak at 154.43 days is clearly visible. Fourth panel: Bayes factor periodogram of the RV residuals after both suspected planets and the activity signal have been modeled and removed. Fifth panel: spectral window function of the combined RV data sets showing a lack of significant peaks that could cause alias signals at the period observed in the RVs.

5.2. Activity Indicators

Plotting the Bayes factor periodograms of the S -index values extracted from the APF and HIRES spectra for HD 216520 reveals a set of peaks in the 20–40 day period range in the Keck HIRES S -index and $H\alpha$ data (see inset panels in Figure 7). Closer inspection shows that none of the HIRES activity peaks overlap directly with the suspected planet signal and that the APF data do not show significant power in this period range, but given the proximity of the HIRES activity peaks, we compare the HIRES RVs to their corresponding S - and H -index values and measure the Pearson correlation coefficients (PCC). The PCC values are 0.12 and 0.22 for the S - and H -index values, respectively, both of which fall below the $\text{PCC} > 0.30$ that is used as the threshold for identifying a moderate linear relationship. These low PCC values suggest that the stellar

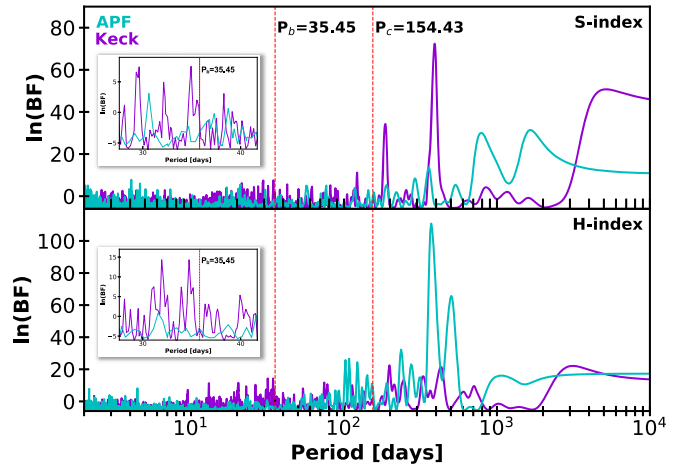


Figure 7. Top: Bayes factor periodogram of the S -index values measured from the APF and Keck HIRES data sets for HD 216520 in cyan and purple, respectively. Inset is a zoomed version focusing on the region around the suspected 35.45 day planet signal. Bottom: same as above, but for the H -index measurements extracted from the APF and Keck HIRES data. The planet period does not overlap with any significant peaks in either the S -index or H -index periodogram.

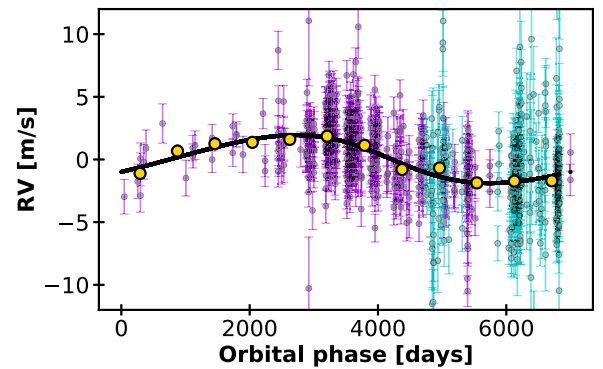


Figure 8. RV observations of HD 216520 phase-folded to the best-fit period of the long-term activity cycle, $P_{\text{act}} = 7767.35$ days, with APF observations shown in cyan and Keck HIRES observations shown in purple. The error bars include the excess white-noise “jitter” from our analysis, and the black solid curve denotes the maximum a posteriori Keplerian model. Yellow points depict the phase-binned RV data.

variability mapped by the S - and H -index indicators is not driving periodicity within the RV data.

Both the HIRES S -index measurements and the combined HIRES and APF RV measurements show evidence of a signal with period, $P \sim 7700$ days, which we take to be a long-term magnetic activity cycle (see Figures 6, 7). The lack of this signal in the APF S -index periodogram is not surprising as the APF data set spans only 2081 days. Fitting a Keplerian model to this long-term signal produces a best-fit period of $P = 7767.35 \pm 1464.31$ days and an RV semiamplitude of $K = 1.90 \pm 0.35 \text{ m s}^{-1}$ (Figure 8). While we believe the signal to be due to stellar variability and not an additional planet, given the overlap in periodicity seen in the combined RV and HIRES S -index data sets, we still included the signal in our overall RV model of the system.

5.3. Photometry and Stellar Rotation

HD 216520 was observed by NASA’s TESS mission (Ricker et al. 2014) during Sectors 18 (UT 2019 November 3–27),

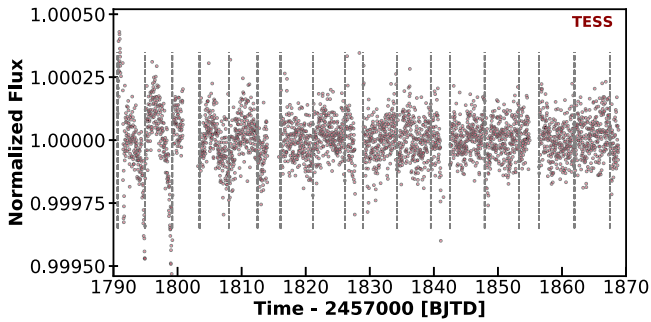


Figure 9. Top panel: three sectors of presearch data conditioned simple aperture photometry (PDCSAP) flux measurements of HD 216520 taken with the TESS spacecraft. The five-day periodicity seen in the light curve is caused by the spacecraft’s regularly scheduled momentum dumps. No signs of stellar periodicity are visible, leaving us unable to discern the star’s rotation period from the TESS data.

19 (UT 2019 November 28–December 23), and 20 (UT December 24–2020 January 21). The star fell on Camera 3 during all three sectors and on CCD 3 in sector 18 and CCD 4 in sectors 19 and 20.

The Science Processing Operations Center (SPOC) data (Jenkins et al. 2016) for HD 216520, available at the the Mikulski Archive for Space Telescopes (MAST) website,²¹ includes the presearch data conditioned simple aperture photometry (PDCSAP) flux measurements (Smith et al. 2012; Stumpe et al. 2012, 2014) shown in Figure 9. At the start of each orbit, thermal effects and scattered light can impact the systematic error removal in PDC (see TESS data release note DRN16 and DNR17). Therefore, we have used the quality flags provided by SPOC to mask out unreliable segments of the time series.

While many of the instrumental variations present in the SAP flux are removed in the PDCSAP result, there are still obvious signs of the spacecraft’s momentum dumps that occur on a roughly five-day period. Beyond the five-day periodicity, we do not see any evidence of rotational modulation in the TESS photometry. Given that HD 216520 has an estimated rotation period of 42–44 days based on its chromospheric activity indicators and rotation–activity–age relations (Section 5), we would expect to see almost two full rotations over the duration of the TESS data. The lack of evident rotation signals therefore further supports the theory that the star is relatively inactive, as suggested by its $\log R'_{\text{HK}}$ values.

5.4. Orbital Parameters

Having established that neither our observational cadence, stellar activity, nor stellar rotation are likely to be the cause of the 35.45 day signal, we now test whether or not the combined RV data provides enough Bayesian evidence to support the existence of the suspect planet. We again apply a statistical model accounting for Keplerian signals and red noise, as well as for correlations between the RVs and the activity indicator data sets (see Section 2). We find that the 35.45 day signal is well supported by the data, with a Bayes factor of $\ln(\text{BF}_5) = 35.37$, again well above the $\ln(\text{BF}_5) = 5$ criteria for being identified as a statistically significant signal.

The resulting fit to the data reveals a two-planet system, where the inner planet has a period of 35.45 ± 0.011 days, a

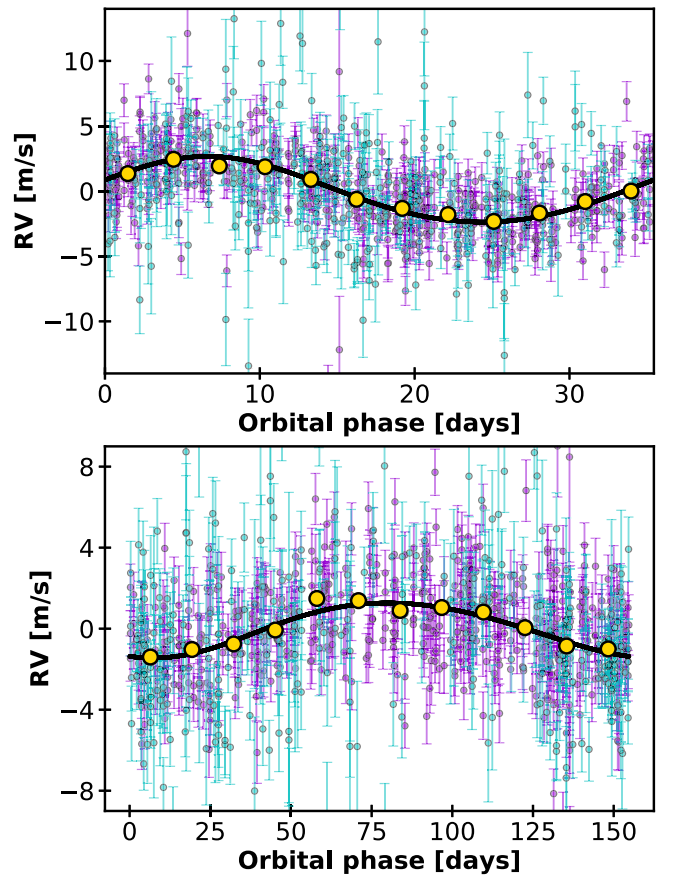


Figure 10. Top panel: RV observations of HD 216520 phase-folded to the best-fit period of planet b, $P_b = 35.45$ days, with APF observations shown in cyan and Keck HIRES observations shown in purple. Bottom panel: same as above, but folded to the best-fit period of planet c, $P_c = 154.43$ days. In both cases, the error bars include the excess white-noise “jitter” from our analysis, and the black solid curve denotes the maximum a posteriori Keplerian model. Yellow points depict the phase-binned RV data.

semiamplitude of $K = 2.28 \pm 0.20 \text{ m s}^{-1}$, and an eccentricity of $e = 0.09 \pm 0.06$, while the outer planet has a period of 154.43 ± 0.44 days, a semiamplitude of $K = 1.29 \pm 0.22 \text{ m s}^{-1}$, and an eccentricity of $e = 0.12 \pm 0.08$ (Figure 10, Table 5). This corresponds to a $10.26 \pm 0.99 M_{\oplus}$ planet on an 0.198 ± 0.0004 au orbit and an $9.44 \pm 1.63 M_{\oplus}$ planet on an 0.528 ± 0.010 au orbit, henceforth referred to as HD 216520 b and HD 216520 c, respectively.

To investigate the persistence of the proposed planetary signal over time, we create a moving periodogram (MP) using the MA(1) noise model of Feng et al. (2017b). The MP is made by constructing Bayesian periodograms for the HD 216520 RV data within a moving time window (see Feng et al. 2017b for a detailed description). In doing so, we find that the 35.45 day signal is detected robustly and repeatedly as more RV data points are added. Indeed, the signal is consistent through an observational baseline that covers more than 90 orbits of the suspected planet and more than nine seasons of ground-based RVs (Figure 11). If RV peaks are long lived and survive over numerous seasons of observation, then stellar activity is generally considered unlikely to be the source of the signal (see, e.g., Buchhave et al. 2016; Pinamonti et al. 2019). As the moving MP does not show evidence of the 35.45 day signal evolving over time nor show a broad distribution of period

²¹ <https://mast.stsci.edu>

Table 5
Best-fit Orbital Solution for Each of the Planets Detailed above and the Activity Signals Noted for HD 190007 and HD 216520

	HD 190007 Planet b	HD 190007 Activity	HD 216520 Planet b	HD 216520 Planet c	HD 216520 Activity	GL 686 Planet b	HD 180617 Planet b
P (days)	11.72 ± 0.001	29.180 ± 0.012	35.45 ± 0.011	154.43 ± 0.44	7767.35 ± 1464.31	15.530 ± 0.0011	105.911 ± 0.109
K (m s^{-1})	5.64 ± 0.55	3.54 ± 0.90	2.28 ± 0.20	1.29 ± 0.22	1.90 ± 0.35	3.004 ± 0.180	2.696 ± 0.224
e	0.14 ± 0.07	0.31 ± 0.15	0.09 ± 0.06	0.12 ± 0.08	0.19 ± 0.12	0.050 ± 0.030	0.101 ± 0.053
ω (deg)	254.64 ± 109.93	225.17 ± 46.98	220.95 ± 125.17	198.12 ± 96.34	95.32 ± 82.22	197.062 ± 153.673	257.433 ± 51.256
M_0 (deg)	100.78 ± 92.27	214.29 ± 46.97	48.72 ± 9.69	194.22 ± 99.71	174.69 ± 53.71	223.884 ± 27.596	123.594 ± 50.897
$\ln(BF_3)$	28.04	7.93	44.3	6.2	6.9	72.03	39.359
$\ln(BF_5)$	23.37	2.68	37.59	-0.52	0.18	65.88	33.062
$m \sin i$ (M_\oplus)	16.46 ± 1.66	...	10.26 ± 0.99	9.44 ± 1.63	...	6.624 ± 0.432	12.214 ± 1.05
a (au)	0.092 ± 0.0008	...	0.198 ± 0.0004	0.528 ± 0.010	...	0.091 ± 0.001	0.343 ± 0.004

Note. Reported values are the mean and standard deviation for each model parameter. The minimum mass and semimajor axis have been estimated by adopting the stellar masses listed for each star in Table 1. M_0 values are referenced to the first RV epoch for each star, which can be found in Appendix B, Tables 6–9.

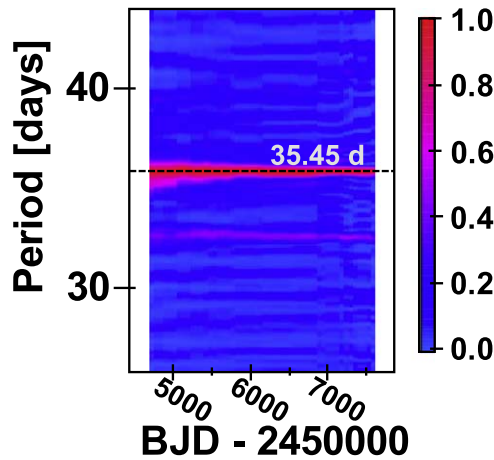


Figure 11. Moving MP-based periodogram for the combined HD 216520 RV data sets. The colors encode the scaled MP power, which is truncated to optimize the visualization of signals. The suspected 35.45 day planet period is denoted with a horizontal dashed lines and shows robust detection through time bins encompassing more than 100 orbits.

measurements over the decade-long RV baseline, as we would expect were it caused by stellar variability, we take this as additional evidence that the signal is not due to surface variability on the host star.

5.5. Transit Search

Using the transit probability equation from Winn (2010), we calculate P_{tra} for each of the HD 216520 planet candidates. For planet b, $P_{\text{tra}} = 1.8\%$, while for planet c, the probability drops to $P_{\text{tra}} = 0.6\%$. Given the planets’ best-fit minimum masses ($10.26 M_\oplus$ and $9.44 M_\oplus$ for planets b and c, respectively) and the conditional distributions for planet radius given a measured planet mass presented in Ning et al. (2018), we would expect these planets to have radii in the $2\text{--}4 R_\oplus$ range. A search of the three sectors of TESS data does not reveal signs of transits for either planet, neither via a traditional box least-squares (BLS) search nor via phase-folding the photometry at the best-fit RV periods.

To test the likelihood that any potential transits may have been missed in the TESS data, we performed an injection and recovery experiment to determine if we could detect these planets assuming they do transit (Figure 12). We use the period posterior derived from the RV data and injected the transits into the SPOC PDCSAP light curves assuming a uniform

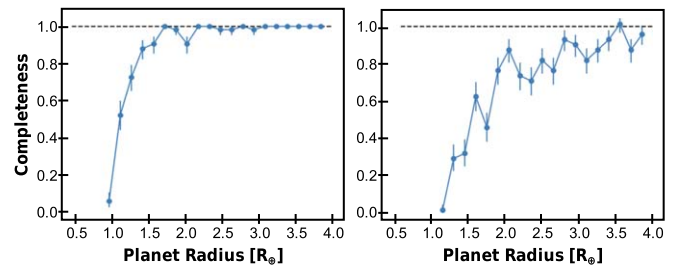


Figure 12. Results of our injection-recovery analysis using the HD 216520 TESS data for planet b (left panel) and planet c (right panel). For planet b, we are able to detect the planet more than 80% of the times when the planet radius is larger than $1.4 R_\oplus$. For planet c, we are able to detect the single transit more than 80% of the times when the planet radius is larger than $2.0 R_\oplus$.

distribution of epochs within the TESS baseline and a uniform distribution of impact parameters. We injected planets over a grid of radii between 1.0 and $4 R_\oplus$, with a step size of $0.15 R_\oplus$. We then detrended the light curves using the Kepler spline (Vanderburg & Johnson 2014) and used the BLS method to search for the transits using the best-fitted RV period. We define a detection of the injected planet if the signal is detected at the correct epoch and with a BLS pink noise-to-signal ratio larger than 10. For planet b, we are able to detect the planet more than 80% of the time when the planet radius is larger than $1.4 R_\oplus$. For planet c, we are able to detect the single transit more than 80% of the time when the planet radius is larger than $2.0 R_\oplus$. Given the expected planet radii, we therefore conclude that planet b does not transit and that planet c did not transit during the observational baseline covered by the TESS photometry.

5.6. Dynamic Stability

A commonly used metric to assess the stability of two-planet systems is the separation of the planets in units of the mutual Hill radius,

$$R_{\text{H,mut}} = \left(\frac{a_1 + a_2}{2} \right) \left(\frac{m_1 + m_2}{3M_*} \right)^{1/3}, \quad (2)$$

where $m_{1,2}$ and $a_{1,2}$ are the masses and semimajor axes of the planets, respectively, and M_* is the mass of the central star. Analytic calculations show that two low-eccentricity, low-inclination planets are “Hill stable,” meaning that they are protected from close encounters for all time, if their spacing

in mutual Hill radii, $\Delta \equiv (a_2 - a_1)/R_{H,\text{mut}}$, exceeds $2\sqrt{3}$ (Gladman 1993; Chambers et al. 1996).

While this criterion is only approximate, the spacing between the HD 216520 planets indicates that stability is likely not a concern. Using MAP parameters, the mutual Hill radius between the two planets is $R_{H,\text{mut}} \approx 0.01$ au, giving a spacing in mutual Hill radii of $\Delta \approx 31.6$.

As another check, we used the N -body integration package rebound (Rein & Liu 2012) to integrate the system for 10^7 orbital periods of the outer planet, i.e., roughly 4.2 Myr. We employed the *whfast* integrator (Rein & Tamayo 2015), using a time step of $0.01 \times$ (inner planet’s period). We see no indications of instability during the course of this integration. Over the course of the integration, the variation in both planets’ semimajor axes is $< 10^{-5}$ au.

6. GJ 686

GJ 686 is a $V = 9.62$ (ESA 1997) M1.5V (Lépine et al. 2013) star $d = 8.157 \pm 0.001$ pc away in Hercules ($\varpi = 122.5609 \pm 0.0346$ mas, Gaia Collaboration et al. 2018; Table 1).²² The star was recently reported to host an $m \sin i = 7.1 \pm 0.9 M_{\oplus}$ planet on a 15.53 day orbit by Affer et al. (2019), and the signal was subsequently confirmed by Lalitha et al. (2019; $m \sin i = 6.24^{+0.58}_{-0.59} M_{\oplus}$). Here we present an updated orbital analysis of the system that includes additional data taken with the APF and PFS, and present an updated minimum mass with 7% uncertainty.

6.1. Radial Velocities

The previously published data sets for GJ 686 include 114 unbinned Keck HIRES velocities (90 individual epochs) from 1997 June to 2013 September, 20 HARPS velocities (19 individual epochs) from 2004 June to 2010 September, 25 SOPHIE velocities obtained from 2007 July to 2009 August, 64 HARPS-N velocities obtained from 2014 February to 2017 October, and 100 velocities obtained with the visible arm of CARMENES from 2016 February to 2018 November. These data are described in detail in Affer et al. (2019) and Lalitha et al. (2019). To these, we add 134 unbinned APF velocities (59 individual epochs) taken from 2013 July to 2016 March and 18 PFS velocities (18 individual epochs) taken from 2012 August to 2017 March. Additionally, we reprocess the HARPS data included in the previous papers using the TERRA pipeline (Anglada-Escudé & Butler 2012) before performing our own orbital fits. Searching the RV periodogram of the combined data set, we find a strong, well-defined peak at $P = 15.53$ days, matching the planet period found in the previously published works, and a lack of potential alias signals in the combined data’s window function (Figure 13). After removing the 15 day signal, we detect an additional signal with a period of $P \sim 2000$ days, which we (like Affer et al. 2019) find to be evidence of a long-term activity cycle based on the Keck and APF activity indicators.

6.2. Photometry and Stellar Rotation

A total of 508 photometric observations were obtained over 7 observing seasons, spanning 2010 through 2016, using the T12 0.8 m APT at Fairborn Observatory. The comparison stars

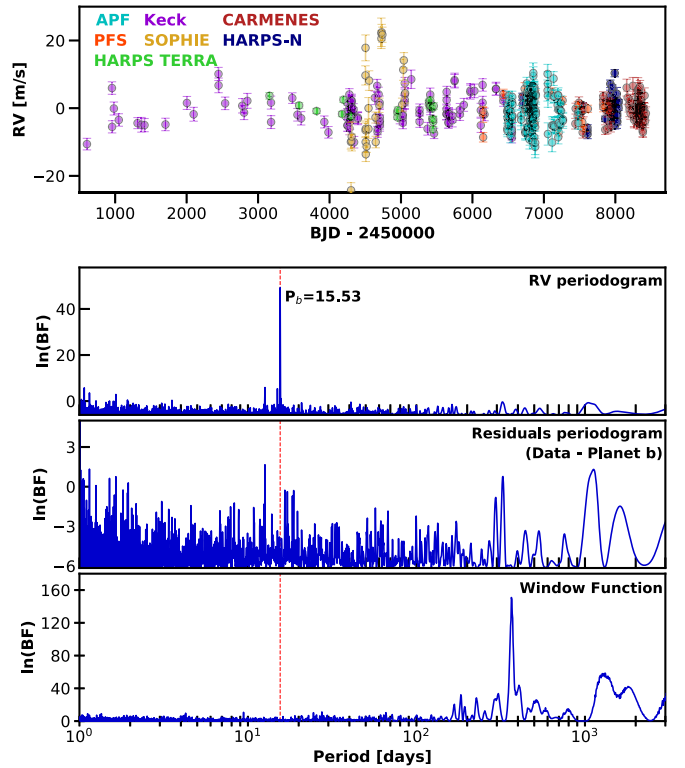


Figure 13. First panel: unbinned RV measurements of GJ 686 color-coded by instrument. Second panel: Bayes factor periodogram of the RV data points showing the peak we detect at 15.53 days. Third panel: residuals periodogram after the 15 day signal has been fitted and removed from the data. Broad peaks in the 1000–2000 day region remain. Fourth panel: spectral window function of the combined RV data sets showing a lack of signals that could cause the 15.53 day signal.

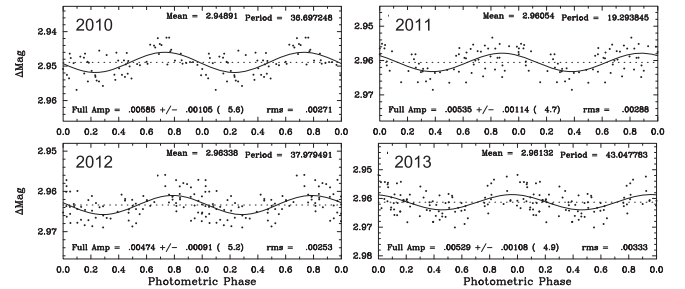


Figure 14. The first four years of GJ 686 photometry, in which we detect coherent rotation signals. From these four data sets we derive a weighted-mean rotation period of 38.732 ± 0.286 days.

used in our data analysis were HD 158806 (an F6IV star with $V = 6.92$, $B - V = 0.46$) and HD 159063 (a G0V star with $V = 6.98$, $B - V = 0.53$). The photometry shows that GJ 686 varies from year to year by roughly $\sim 1\%$, consistent with low to moderate activity. When searching the photometric data for periodicity, we find significant signals only in the first four seasons. The star appears to be “double spotted” in 2011, cutting the observed photometric period in half. A weighted mean of the four photometric periods (doubling that from the 2011 observing season) gives us a value of 38.732 ± 0.286 days (Table 1, Figure 14), which we take to be our best estimate of the stellar rotation period. We note that this is well separated from our proposed new planetary period.

²² The proximity of GJ 686 was first reported and its parallax measured (108 ± 11 mas) by Slocum & Mitchell (1913).

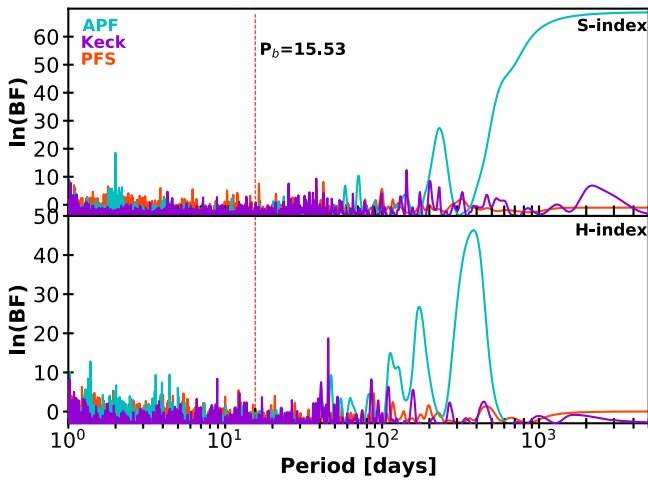


Figure 15. Top: Bayes factor periodogram of GJ 686 using the S -index values measured from the APF, Keck HIRES, and PFS data sets in cyan, purple, and orange, respectively. There are no prominent peaks in the vicinity of the 15.53 day planet period. Bottom: same as above, but for the H -index measurements extracted from the Keck HIRES and PFS data in purple and orange, respectively.

6.3. Activity Indices

When plotting the S - and H -index Bayes factor periodograms using measurements extracted from our APF, HIRES, and PFS spectra for GJ 686, we find that none of the periodograms of the various activity data sets show peaks at or near the 15.53 day planet period (Figure 15). We do, however, see a peak at $P = 40.8$ days, which is in rough agreement with the stellar rotation period we measure, and those presented by Affer et al. (2019, $P_{\text{rot}} = 36.7$ days) and Lalitha et al. (2019, $P_{\text{rot}} = 38.4$ days). When considering the 2000 day signal, which the HIRES S -index data shows clearly at the $\ln(\text{BF}_5) \sim 10$ level, we note that of the individual stellar activity data sets, only the Keck HIRES indicators covers a long-enough time baseline to be sensitive to such a long-period sinusoid. We identify this signal as a likely long-period magnetic cycle, and with a period of ~ 5.5 yr it aligns well with the typical long-term variability timescales for early to mid M-dwarfs (Gomes da Silva et al. 2012; Suárez Mascareño et al. 2017).

6.4. Orbital Parameters

Unsurprisingly, given its status as a previously published planet, we find that the 15.53 day signal is well supported by the combined RV data sets, with $\ln(\text{BF}_5) = 65.88$. The resulting fit to the data reveals a planet with a period of 15.53 days, a semiamplitude of $K = 3.004 \text{ m s}^{-1}$, and an eccentricity of $e = 0.050$ (Figure 16, Table 5). This corresponds to a $6.624 M_{\oplus}$ planet orbiting 0.091 au from its host star. These values are in good agreement with the previously published detections of GJ 686 b, and our RV semiamplitude matches the smaller value measured in Lalitha et al. (2019, $K = 3.02_{-0.20}^{+0.18} \text{ m s}^{-1}$) more closely than the value measured by Affer et al. (2019, $K = 3.29_{-0.32}^{+0.31} \text{ m s}^{-1}$).

7. HD 180617

HD 180617 is an M3 dwarf star located just under 6 pc away from the Sun (Gaia Collaboration et al. 2016). The star was

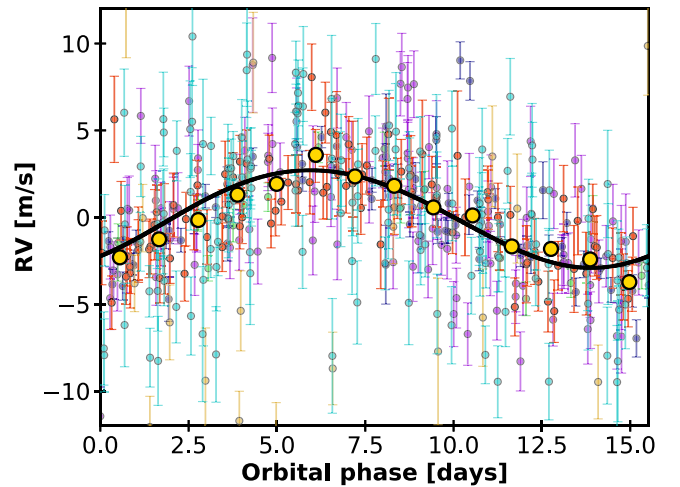


Figure 16. Top panel: RV observations of GJ 686 (colors match those in Figure 13) phase-folded to the best-fit period of $P = 15.53$ days. The error bars include the excess white-noise “jitter” from our analysis, and the black solid curve denotes the maximum a posteriori Keplerian model. Yellow points depict the phase-binned RV data.

recently found to host a $12.2 m \sin i$ planet on a 105.9 day orbit using data from Keck HIRES, HARPS, and CARMENES (Kaminski et al. 2018). Here we present an updated orbital fit that incorporates an additional 126 RV measurements taken with the APF between 2013 and 2019 July.

7.1. Radial Velocities

The published RV data sets for this star include 158 unbinned HIRES velocities (134 individual epochs) taken from 2001 June to 2014 September, 108 HARPS velocities taken before the fiber upgrade, 40 HARPS velocities taken after the fiber upgrade, and 124 CARMENES velocities. These RV data sets have mean uncertainties of 2.57, 0.85, 0.45, and 1.59 m s^{-1} , respectively, and are described in detail in Kaminski et al. (2018). The APF data included here is comprised of 126 RV measurements (58 individual epochs) taken between 2013 and 2019 July that have a mean uncertainty of 1.65 m s^{-1} . Searching the combined data set, we find a strong, well-defined peak in the RV periodogram at $P = 105.91$ days, which is consistent with the planet period detected in Kaminski et al. (2018), and a corresponding lack of signals in the combined RV window function that could cause the RV peak (Figure 17).

7.2. Activity Indicators

S - and H -index activity indicators were extracted from each of the HIRES and APF spectra using the methods described in Section 2 (Figure 18). We find no significant peaks at the period of the planet ($P = 105.91$ days); however, the data from the APF do include large peaks at ~ 200 days, which match a peak seen in indicators sensitive to line-profile variations described in Kaminski et al. (2018).

7.3. Photometry and Stellar Rotation

A total of 707 observations were obtained between 2009 through 2017 using the T10 0.8 m APT at Fairborn Observatory. The comparison stars used in the photometric analysis were HD 183085 (an F2V star with $V = 6.72$, $B - V = 0.36$) and HD 180945 (an F5V star with $V = 7.15$

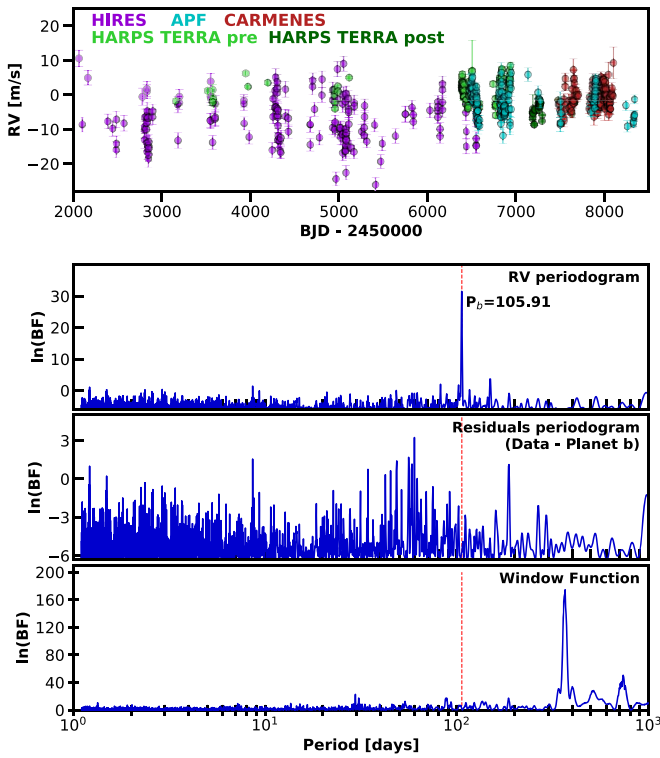


Figure 17. First panel: unbinned RV measurements of HD 180617 taken with the APF (cyan), Keck HIRES (purple), and HARPS (green). Second panel: Bayes factor periodogram of the RV data showing the planet’s peak at 105.91 days. Third panel: residuals periodogram after the 105.91 day signal has been fitted and removed. Fourth panel: window function of the combined RV data set showing a clear lack of significant peaks at the proposed planet period.

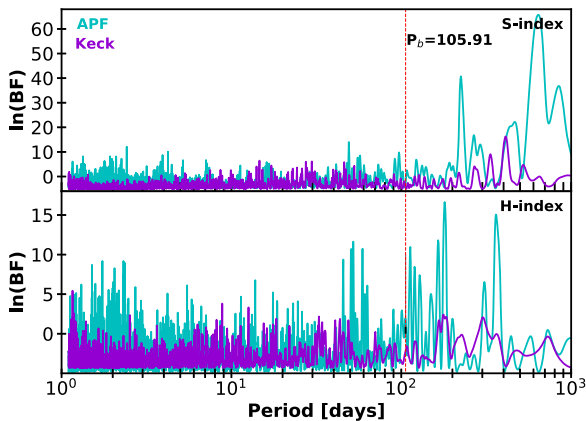


Figure 18. Top: Bayes factor periodogram of the S -index values of HD 180617 measured from the APF and Keck HIRES data sets in cyan and purple, respectively. There are no prominent peaks in the vicinity of the 105.91 day planet period. Bottom: same as above, but for the H -index measurements extracted from the APF and Keck HIRES spectra, which also show a lack of peaks at the planet’s period.

and $B - V = 0.47$). We analyze each observing season for rotation and find periods for all nine seasons, with the star appearing to be “double spotted” in 2010 and 2015. In those two years, the rotation period is taken to be twice the observed photometric period. Combining the results across all nine seasons produces a weighted-mean rotation period of 50.60 ± 0.41 days (Figure 19).

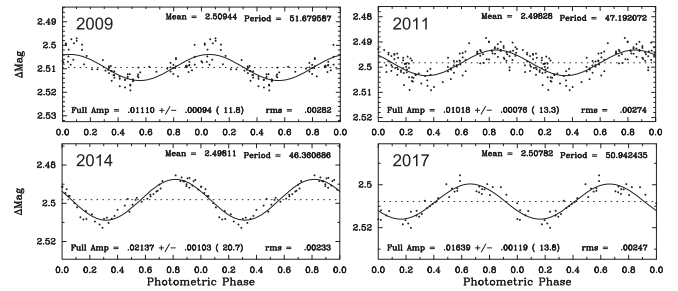


Figure 19. APT photometry for four of the nine seasons during which HD 180617 was observed. Combining the results across all nine seasons produces a weighted-mean rotation period of 50.60 ± 0.41 days.

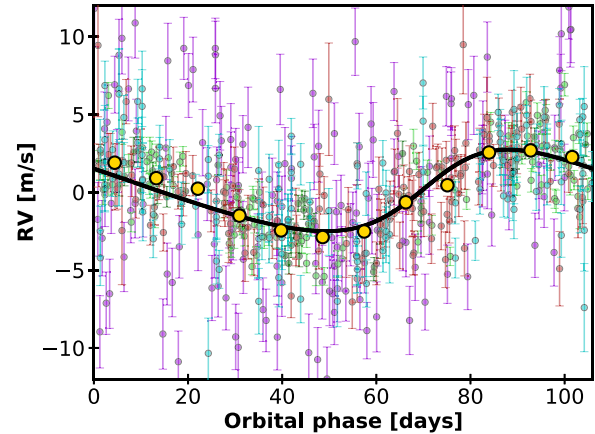


Figure 20. RV observations of HD 180617 phase-folded to the best-fit period of $P = 105.91$ days (colors match those in Figure 17). The error bars include the excess white-noise “jitter” from our analysis, and the black solid curve denotes the maximum a posteriori Keplerian model. Yellow points depict the phase-binned RV data.

7.4. Orbital Parameters

We find that the best orbital fit to the combined RV data set for HD 180617 is a mildly eccentric ($e = 0.101$), $P = 105.91$ day orbit with a semiamplitude $K = 2.696 \text{ m s}^{-1}$ (Figure 20). This corresponds to a $12.214 M_{\oplus}$ mass planet in a 0.343 au orbit around the host star, consistent with the findings of Kaminski et al. (2018). A search of the RV residuals periodogram does not reveal any evidence for additional signals.

8. Discussion

In this study, we analyzed 34 Keck HIRES and 157 APF RV measurements of the K4V star HD 190007 along with 504 Keck HIRES and 300 APF RV measurements of the K0V star HD 216520. From these analyses, we detect three new planets. Based on our derived orbital parameters, HD 190007 b and HD 216520 b are both close-in, sub-Neptune-type planets while HD 216520 c is a longer period, temperate sub-Neptune planet. We also confirmed the orbital parameters of two previously published low-mass planets. First, we derived an updated orbital solution for the planet orbiting the M1.0V star GJ 686 reported by Affer et al. (2019) and Lalitha et al. (2019) using an additional 134 new RV APF measurements and 18 new PFS measurements. And second, we updated the orbital solution of the planet orbiting the M3.0V star HD 180617 detailed in

Kaminski et al. (2018), adding 126 new APF measurements to the combined data set.

8.1. Benefits of Long-baseline, Multifacility Data Sets

K- and M-dwarf stars make enticing RV survey targets because (1) their lower stellar masses result in larger RV semiamplitudes from an exoplanet with a set period and mass than would be induced on hotter, more massive stellar types, and (2) their lower effective temperatures result in a higher number of stellar absorption lines that increase the RV information content in their spectra (Beatty & Gaudi 2015). While, to our knowledge, HD 190007 and HD 216520 have only been included in the Keck HIRES and APF surveys described here, GJ 686 and HD 180617 have each been targeted by at least four independent surveys.

This array of data sets spanning long temporal baselines allows for the derivation of very precise orbital models for each of the planets and also for the comparison of both planetary and stellar variability detections between different instruments and facilities. Our final orbital and planetary parameters for each of the planets are summarized in Table 5. Each of the planetary $m \sin i$ values is determined to the $\sigma_K \geq 10$ level, a benefit of having many precise RV observations taken over extended baselines. When comparing to the confirmed planets listed on the Exoplanet Archive, less than a quarter (roughly 22%) of RV detected, sub-Neptune-mass planets have $m \sin i$ measured to this level. Planets with such precise $m \sin i$ values offer some of the best insights and constraints when modeling the formation, evolution, and dynamic interactions of planetary systems. Having such long-baseline results that accurately constrain the stars' RV signal could also allow for the detection of N -body effects such as planet–planet scattering with more comprehensive modeling, similar to the use of transit timing variations in transit data.

We find that our final results for the previously published planets, GJ 686 b and HD 180617 b, are in good agreement with the earlier results found in Kaminski et al. (2018), Affer et al. (2019), and Lalitha et al. (2019). For both planets, our derived planet periods, eccentricities, semiamplitudes, and $m \sin i$ values are all within the 1σ uncertainties across all three existing publications.

One particular strength of the APF telescope, with its ability to achieve nightly cadence on interesting RV target stars, is that the resulting data can help disentangle observational aliases. In particular, earlier versions of the HD 190007 data set showed strong signals at periods of both 11.72 and 1.09 days, which are daily aliases of one another. For example, earlier versions of the RV periodogram for HD 190007 showed that an additional peak appeared at $P = 1.09$ days, corresponding to the 1 day alias ($f_{1.09 \text{ days}} = f_{11.72 \text{ days}} + f_{1 \text{ day}}$) of the 11.72 day signal. We had reason to suspect that the longer period signal was the true signature of the planet because the 1.09 day signal produced a notably lower $\ln(\text{BF}_5)$ value and required an orbital eccentricity of $e = 0.119 \pm 0.068$. This nonzero eccentricity seemed unlikely for a planet on such a short period orbit, which we would expect to have circularized via tidal dissipation (Van Eylen & Albrecht 2015; Hadden & Lithwick 2017). But it was challenging to make a robust determination of which signal was caused by the planet and which was the alias. By observing the star for an additional season and ensuring that it underwent high-cadence observations (Figure 1), we were able to update the analysis and found that the 1.09 day signal had dramatically

decreased in significance, further strengthening our argument that the 11.72 day signal presented here is the true Keplerian signature of the planet. This same effect of being able to discern between true signals and observational aliases can be achieved by combining data from different facilities that have some degree of longitudinal spread across the globe. This enables a broader range of short-period observational cadences based on telescope separations and will help remove power from the 1 day alias that plagues single-site observations.

8.2. Potential for Additional Detection Methods

Having discovered these planets via the RV method, we investigate whether they might make good candidates for additional detection/characterization methods such as transit, astrometric, and direct imaging observations. We calculate transit probabilities using Winn (2010), and astrometric semiamplitudes and maximum projected separations using Perryman (2011). We find that due to the combination of low mass and relatively short orbital periods, none of the five planets detailed in this work are expected to produce an astrometric semiamplitude larger than 5 mas, placing them all beyond the reach of Gaia's detection threshold. Similarly, the projected on-sky separation of the HD 190007, HD 216520, and HD 180617 planets from their host stars are all below $0''.03$, making them inaccessible to even the upcoming generation of Extremely Large Telescopes. GJ 686 b is a slightly more promising case, with a maximum projected separation of $0''.058$, but even this is on the very edge of performance expected from ground-based, 30 m class facilities.

In order to calculate the planets' transit probabilities, we need to make an assumption about their sizes. We compare the minimum masses listed in Table 5 with the conditional distributions for a planet's radius given its mass presented in Figure 7 of Ning et al. (2018). We adopt a uniform radius assumption of $R = 3 R_{\oplus}$ for all of our planets as they correspond most closely to the mass = $10 M_{\oplus}$ distribution. Inserting this radius assumption along with the planets' measured orbital parameters into Equation 9 of Winn (2010) produces transit probabilities well below 1% for each of the planets.

Thus, while the RV detections for all of these systems are robust, we do not expect any of these planets to be particularly well suited to additional methods of detection and characterization.

8.3. Comparison to Close-in Kepler Multiplanet Systems

With minimum masses just at or below that of Neptune and periods in the 10–100 day range two of the planets discovered here (HD 190007 b and HD 216520 b) are also reminiscent of the numerous super-Earth and sub-Neptune planets detected in transit by the Kepler mission (Figure 21). In particular, Kepler revealed that about half of stars in our galaxy harbor the small ($R_p \leq 4 R_{\oplus}$), close-in ($P \leq 100$ days) planets, which are often found in tightly spaced, multiplanet systems (Latham et al. 2011; Lissauer et al. 2011, 2014; Rowe et al. 2014). Most surprisingly, the multiple planets in the same systems tend to be similar in both mass and radius (Millholland et al. 2017; Wang 2017; Weiss et al. 2018).

That is, statistically speaking, for a given short-period super-Earth or sub-Neptune planet, like HD 190007 b or HD 216520 b, we would expect the existence of additional close-in planets and for those planets to have orbital periods and masses similar

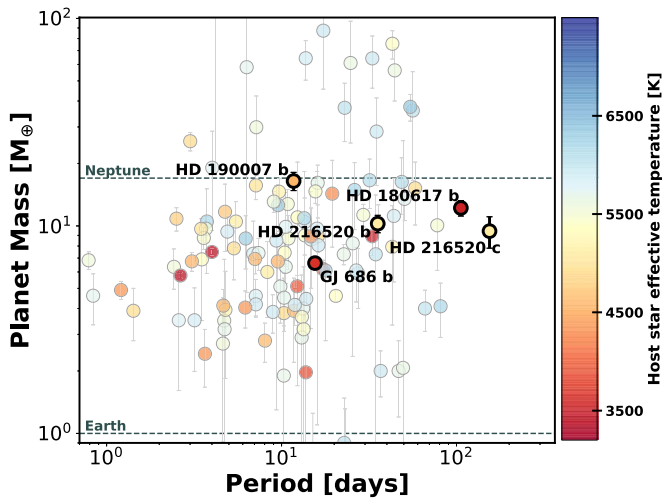


Figure 21. Out of the 136 Kepler and K2 sub-Neptune-mass exoplanets that have orbital periods less than 100 days, 116 (85%) are in multiplanet systems. Our three new and two updated planets, labeled here in black, land in a very similar region of period–mass parameter space as the Kepler multiplanet systems. If the planets in this paper were formed in a similar manner as the ones found by Kepler, this would suggest that additional, close-in, and similar-mass planets may be present in those systems. Note that our the new planets have only minimum mass measurements, as their inclinations are unknown, and so their positions on this plot are lower limits.

(within a factor of 2) to that of the detected planet. While HD 216520 c is very similar in mass to HD 216520 b, much like the multiplanet systems found with Kepler, it does not have an orbital period within a factor of 2 of the inner planet as would be expected for a Kepler multiplanet system.

We therefore examine the possibility that there may be additional planets orbiting HD 190007 and HD 216520 with periods less than 100 days. Neither star’s data set shows evidence of additional, significant signals in their respective RV residuals periodogram (Figures 1 and 6). Yet this does not rule out the possibility that additional signals might be present at significance levels obscured by effects from stellar activity, our observing cadence, and our RV precision, among others. To test our data sets’ ability to detect such signals, we perform an injection and recovery test using the same residual RVs used to create those periodograms. First, we define period and semiamplitude ranges similar to those of the small, close-in planets detected by Kepler: $0.5 < P < 300$ days and $0.5 < K < 10 \text{ m s}^{-1}$. We then randomly draw a period and semiamplitude value from a log distribution bounded by these end points and inject the corresponding Keplerian signal into the RV residuals. We generate a Lomb–Scargle periodogram of the resulting RVs and calculate the False Alarm Probability (FAP) of the periodogram at the highest peak within 10% of the injected period. We define our recovery criteria such that cases when the resulting FAP value is below 0.01 are considered to be successful detections of the planet. We execute this process 100,000 times for each star’s residuals data sets and visualize the results in Figure 22. The cool colored regions of the plot (FAP < 0.01) represent period and semiamplitude combinations that we successfully recover. We note here that this process is an estimate of our ability to detect a periodic signal with a certain period. This is not the estimate of our probability of recovering a Keplerian signal. Finding a periodic signal is a step in that process, so our detection probabilities are likely

overestimates of our ability to actually recover and characterize a planet’s orbit.

In the case of HD 190007, for which we have 123 RV epochs taken over two decades, we are sensitive to planets with semiamplitudes down to $\sim 3 \text{ m s}^{-1}$ for periods out to one year. Given the star’s mass, the 3 m s^{-1} sensitivity level corresponds to planets in the $4\text{--}28 M_{\oplus}$ range. As HD 190007 b has an $m \sin i$ value of $16.46 M_{\oplus}$ we are most interested in our ability to detect “similar” planets like those we would expect to see in a Kepler-like system, which would fall in the $8\text{--}30 M_{\oplus}$ mass range. While planets with masses $\geq 20 M_{\oplus}$ should be detectable throughout the 1–100 day period range populated by the close-in Kepler multiplanet systems, those in the $8\text{--}20 M_{\oplus}$ range could be obscured at periods longer than 10 days.

For HD 216520, with its 369 RV epochs taken over 19 years, the injection/recovery process suggests that we are sensitive to planets with semiamplitudes down to $\sim 1 \text{ m s}^{-1}$ for periods out to 300 days. A 1 m s^{-1} signal in the HD 216520 data set corresponds to a planet with mass ranging from 1.5 to $10 M_{\oplus}$ when considering periods less than 300 days. Given the $11.63 M_{\oplus} m \sin i$ value of HD 216520 b, and again assuming that Kepler-like systems will have planets of similar masses, we would expect any additional planets in the system to have masses in the $5\text{--}20 M_{\oplus}$ range, making it likely that we would have noticed their presence in our existing data.

Similar to our solar system, the Kepler multiplanet systems tend to be well organized—they have small mutual inclinations, circular orbits, and are generally well aligned with the host star’s rotation. Because both HD 190007 b and HD 216520 b are on circular orbits, additional coplanar planets within these systems should be able to survive on similarly circular orbits beyond the Hill stability threshold. But as seen above, we rule out the presence of additional, close-in planets with masses similar to our newly detected planets in tightly spaced stable orbits.

One possibility is that because RV detections measure a planet’s minimum mass and not its true mass, then one or both of these planets may actually be a more massive, gas giant on a highly inclined orbit. Gas giants are significantly less likely to be accompanied by either other close-in planets (Steffen et al. 2012; Cañas et al. 2019), or planets with similar masses (Wang 2017). HD 216520 in particular has an extremely small reported $v \sin i$ ($0.2 \pm 0.05 \text{ km s}^{-1}$) compared with stars that have similar T_{eff} (5082 K), lending some credence to the idea that the planet’s orbital plane is far from the line of sight. As the orbits of most small planets align with their host star’s equator (Winn & Fabrycky 2015; Wang et al. 2018), HD 216520’s small $v \sin i$ value suggests that the planet is likely to be a highly inclined gas giant, otherwise the projected RV is too small to be detected. But while we selected the Brewer et al. (2016) $v \sin i$ value for consistency with the other stellar parameters reported in Table 1, there are two additional $v \sin i$ measurements for this star in the literature. Luck (2017) reports a $v \sin i$ value of 2.5 km s^{-1} while Mishenina et al. (2008) find $v \sin i = 1.4 \text{ km s}^{-1}$. If one of these larger values is a more accurate measurement of the HD 216520’s rotational velocity, which seems reasonable given the star’s T_{eff} , then it would be less likely that HD 216520 b is a gas giant masquerading as a Neptune.

An alternate explanation is that the planets detected in this paper using the RV technique and the planets detected by Kepler are not from the same population and therefore do not

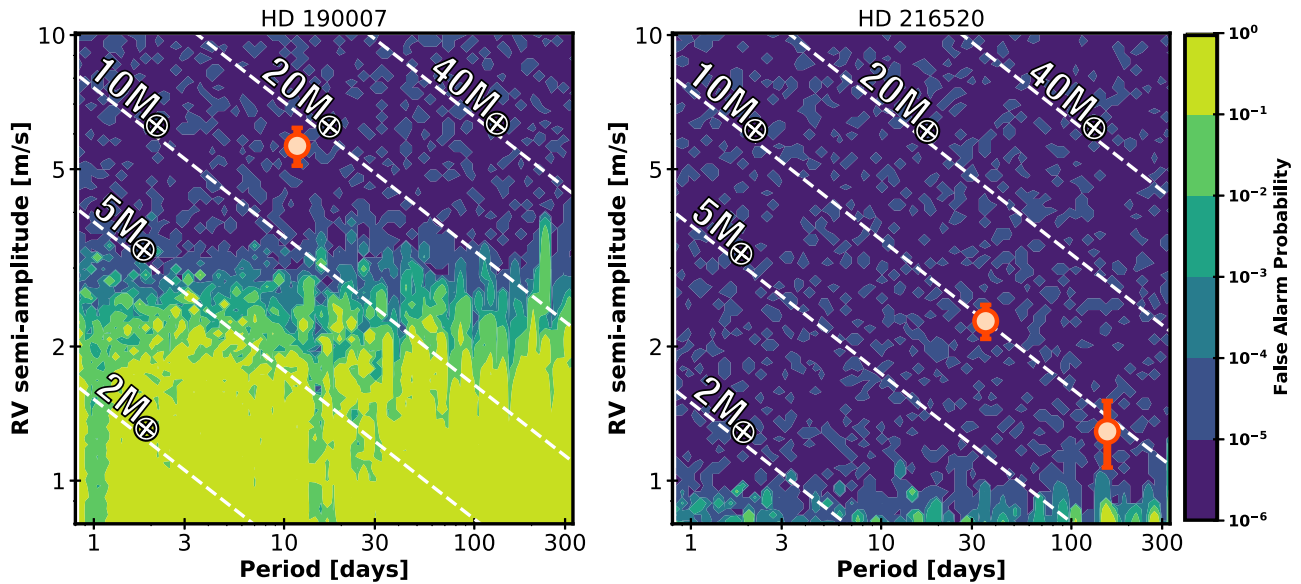


Figure 22. Injection and recovery contour maps for HD 190007 (left) and HD 216520 (right), with the newly discovered planets shown as orange circles. Coloration represents the FAP value of the LS periodogram at the injected period, with the darker colors (FAP < 0.01) representing planets that were successfully recovered. White lines show the RV semi-amplitude of a given planet mass as a function of period. For HD 190007, we are sensitive to planets with masses greater than 5–20 M_{\oplus} depending on the period, while for HD 216520, we are sensitive to planets with masses greater than 1–10 M_{\oplus} . The lack of a discovery of planets of similar mass and period in these systems is in marked contrast with Kepler discoveries, where $\sim 85\%$ of planets have neighbors that are close in mass, radius, and period.

share similar observational properties. There is an unsolved discrepancy of the hot-Jupiter occurrence rate between the Kepler and RV samples, which is partially attributed to the fact that the Kepler sample has lower metallicity than the RV sample (Guo et al. 2017) as the RV technique performs better on high-metallicity stars because of the increased information content in their stellar spectra. As pointed out by Brewer et al. (2018), super-Earth/sub-Neptune’s multiplicity is anticorrelated with host stellar metallicity. Metal-rich stars, HD 190007 for example ($[\text{Fe}/\text{H}] = 0.16 \pm 0.05$), are less likely to host multiple-planet systems. This raises the interesting possibility that our two new planets detected here have followed a different path of planet formation than that taken by the majority of Kepler planets. Though our work has a small sample size, the addition of even a small number of planets helps to point the way toward a future verification or rebuttal of this picture.

The research was carried out in part at the Jet Propulsion Laboratory, California Institute of Technology, under a contract with the National Aeronautics and Space Administration (80NM0018D0004).

The work herein is based on observations obtained at the W. M. Keck Observatory, which is operated jointly by the University of California and the California Institute of Technology, and we thank the UC-Keck and NASA-Keck Time Assignment Committees for their support. We also wish to extend our special thanks to those of Hawaiian ancestry on whose sacred mountain of Maunakea we are privileged to be guests. Without their generous hospitality, the Keck observations presented herein would not have been possible. The work herein is also based on observations obtained with the Automated Planet Finder (APF) telescope and its Levy

Spectrometer at Lick Observatory, along with data gathered with the 6.5 m Magellan Telescopes located at Las Campanas Observatory, Chile. G.W.H. acknowledges long-term support from NASA, NSF, Tennessee State University, and the state of Tennessee through its Centers of Excellence program.

This research has made use of the Keck Observatory Archive (KOA), which is operated by the W. M. Keck Observatory and the NASA Exoplanet Science Institute (NExScI), under contract with the National Aeronautics and Space Administration. We specifically acknowledge the 83 RVs used in the analysis of HD 216520 that are based on spectra taken by the California Planet Search team and archived in the Keck Observatory Archive. This research has made use of the SIMBAD database, operated at CDS, Strasbourg, France.

This publication makes use of VOSA, developed under the Spanish Virtual Observatory project supported by the Spanish MINECO through grant Aya2017-84089. VOSA has been partially updated by using funding from the European Union’s Horizon 2020 Research and Innovation Programme, under grant agreement No. 776403 (EXOPLANETS-A).

Simulations in this paper made use of the REBOUND code which is freely available at <http://github.com/hannorein/rebound>.

Facilities: UCO/Lick: The APF (Levy spectrograph), Magellan: Clay (Planet Finder Spectrograph), Keck I: (HIRES), TSU:AST (T4 and T12 APTs).

Appendix A Bayes Factor Periodograms

Figures 23–26 below depict the full set of Bayes factor periodograms for each of the four stars included in this study.

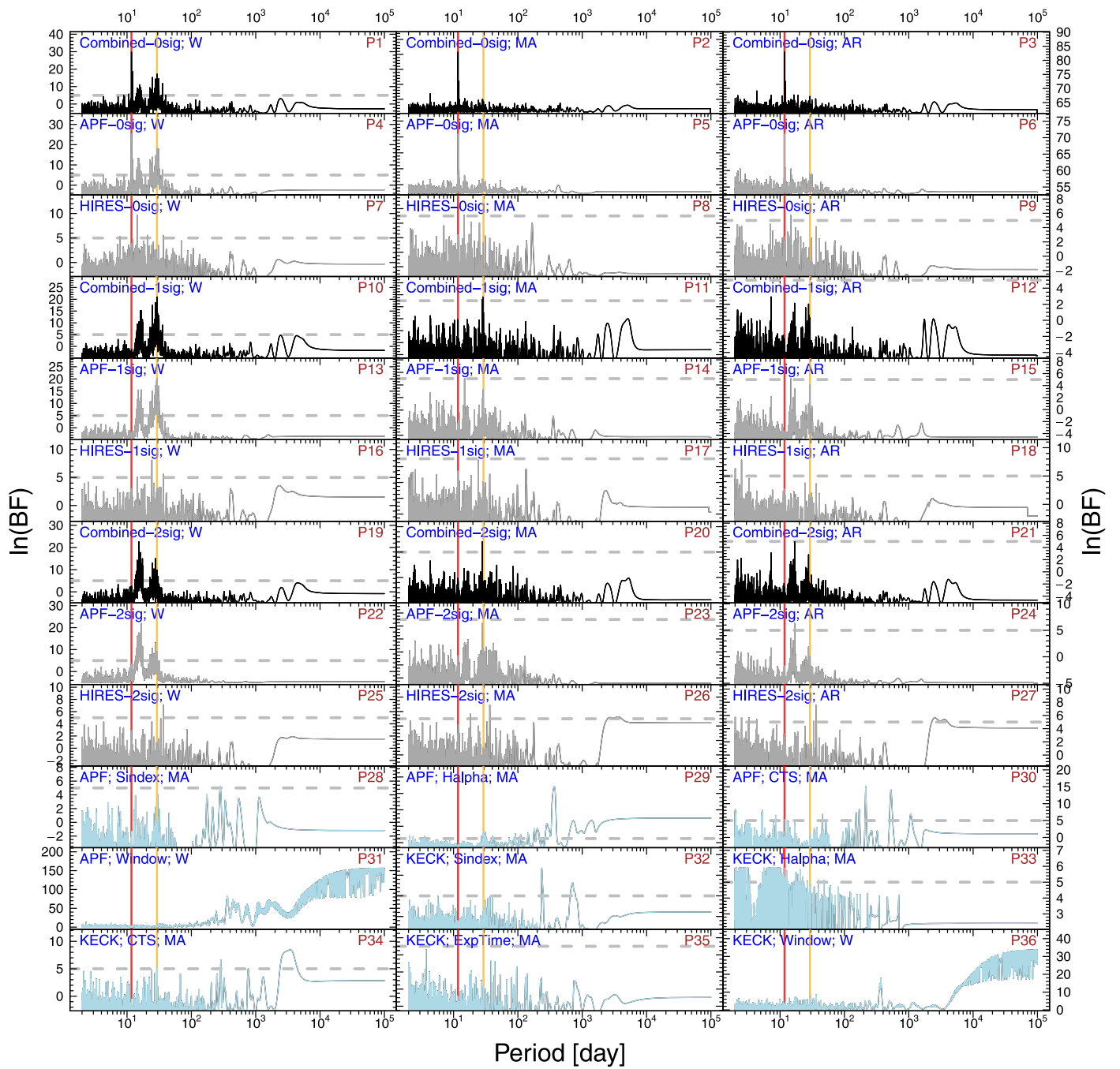


Figure 23. Full set of Bayes Factor Periodograms for HD 190007. The red line denotes the 11.72 day signal that we take to be the true planet signal, while the gold line shows the 29 day period that we find to be caused by stellar variability.

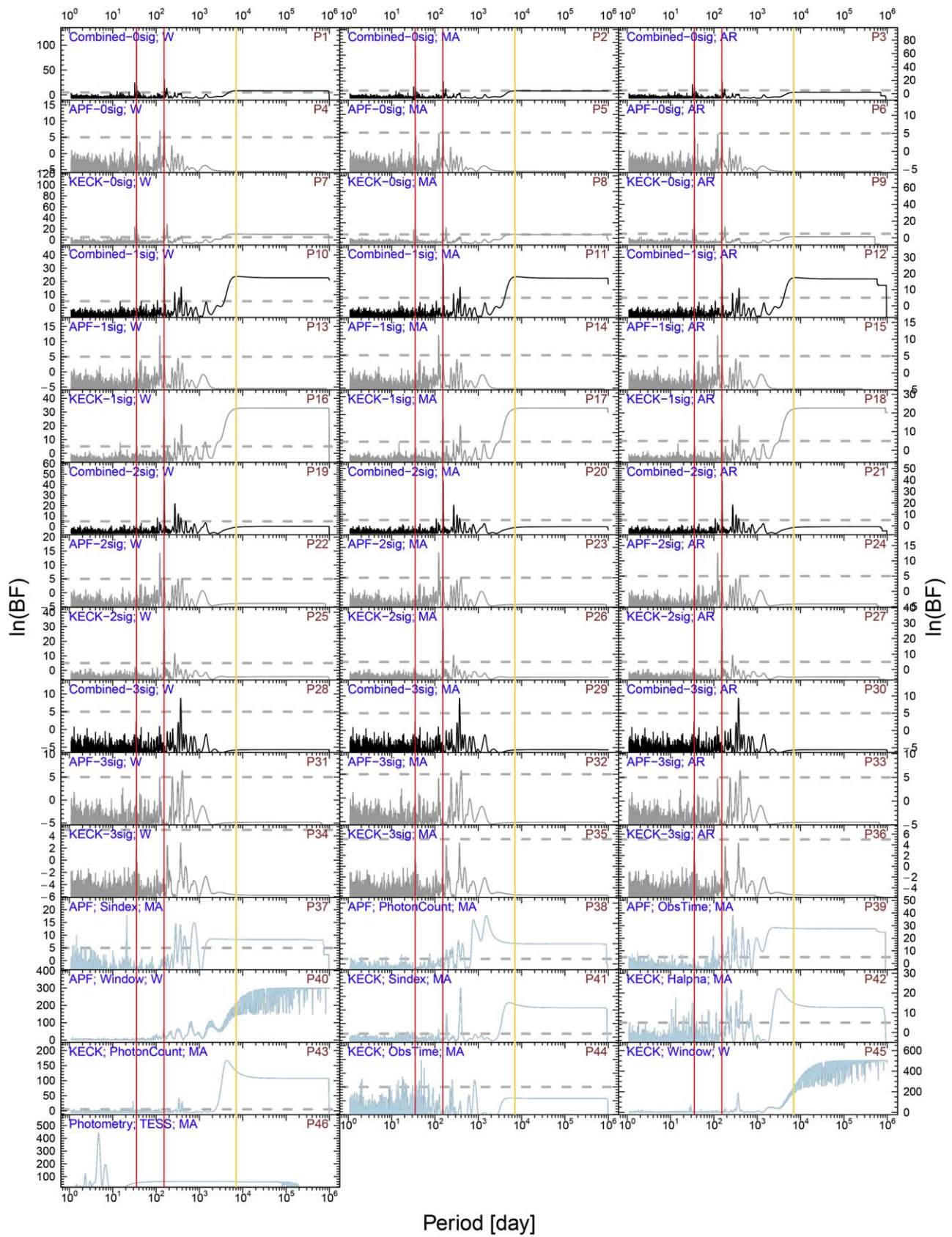


Figure 24. Full set of Bayes Factor Periodograms for HD 216520. The red lines denote the 35.45 and 154.43 day signals that we take to be planets. The gold line shows the additional 7767.35 day signal that we believe to be caused by the star’s magnetic activity cycle.

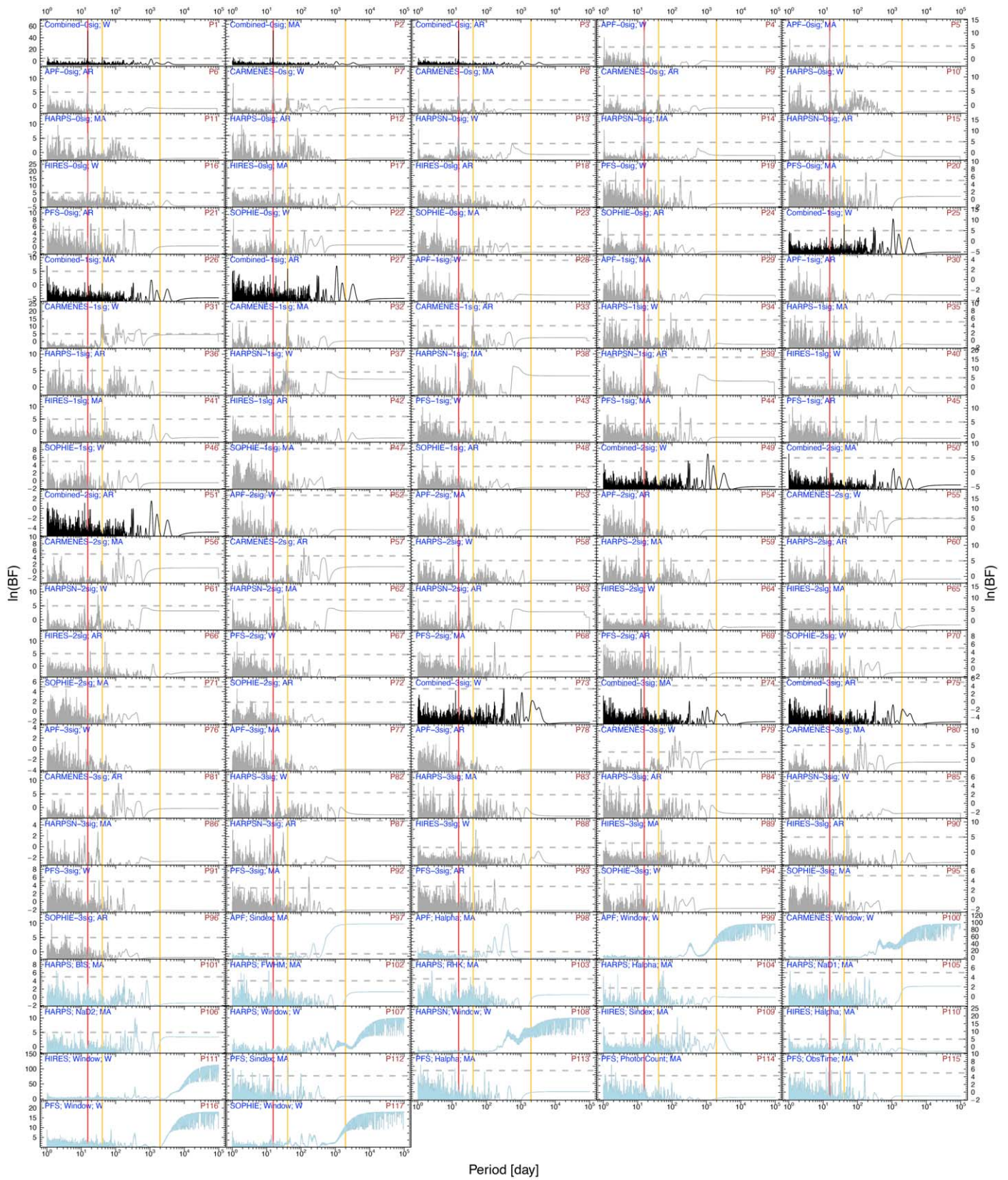


Figure 25. Full set of Bayes Factor Periodograms for GL 686. The red line denotes the 15 day planet signal originally identified in Affer et al. (2019) and Lalitha et al. (2019) and confirmed again in this work. The gold lines show the ~ 40 day and ~ 2000 day signals that we identify as the star’s rotational and magnetic activity cycles, respectively.

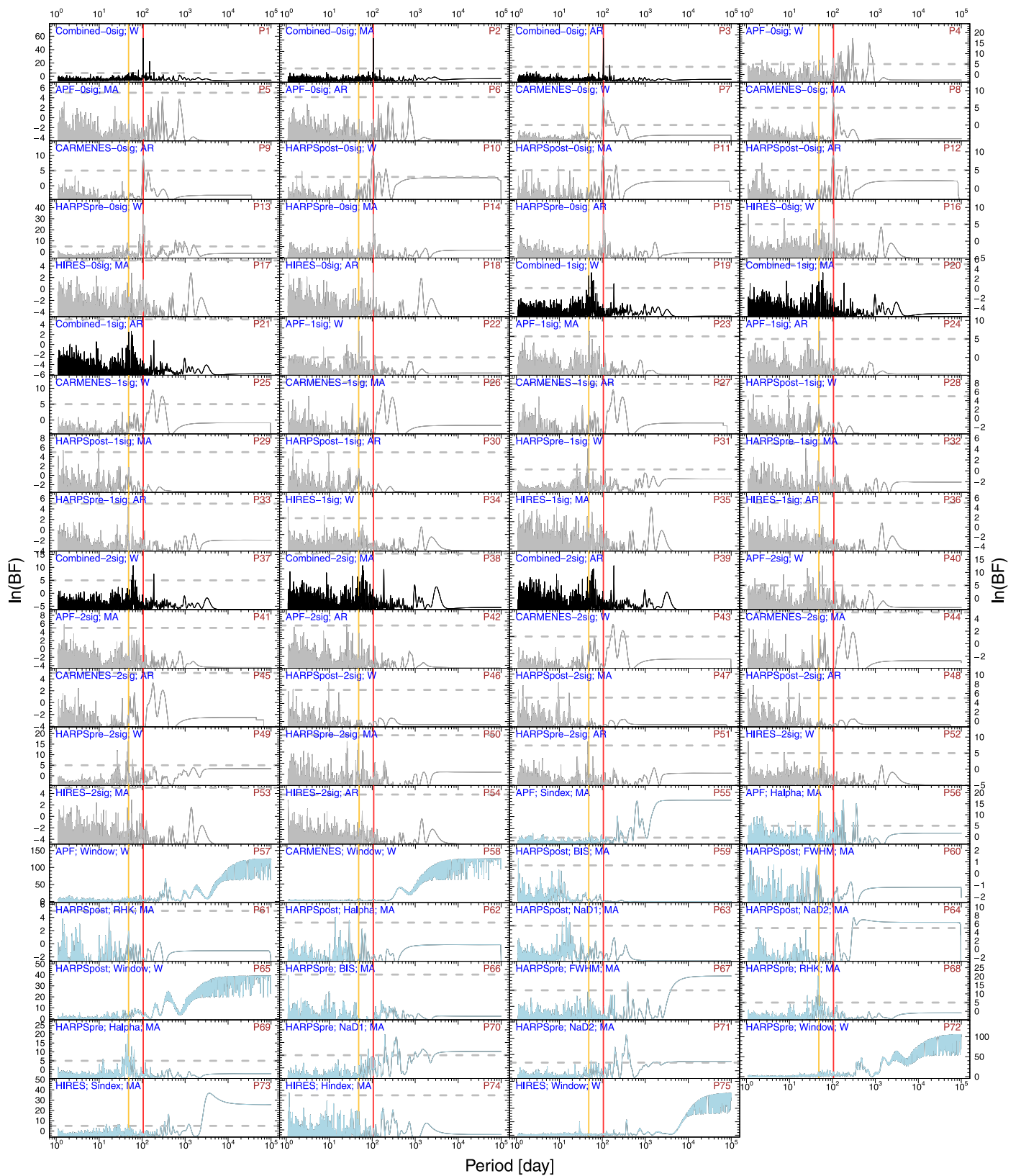


Figure 26. Full set of Bayes Factor Periodograms for HD 180617. The red line denotes the 105.91 day planet signal originally identified in Kaminski et al. (2018) and confirmed in this work. The gold line shows the ~ 50 day activity signal seen in the HARPS H- α measurements and the APT photometry that we take to be the star’s rotation period.

Appendix B

Radial Velocity Measurements

Tables 6–9 contain the new RVs from HIRES, the APF, PFS, and HARPS-TERRA presented in this paper. A portion of

each table is shown here for guidance regarding their forms and content, while the full tables are published in machine-readable format.

Table 6
Radial Velocity Data for HD 190007

MJD	RV (m s ⁻¹)	σ_{RV} (m s ⁻¹)	S Index	H Index	Instrument
2450984.05436	7.41	1.33	0.7281	-1	HIRES
2451013.94476	-1.73	1.46	0.6926	-1	HIRES
2451050.86802	-6.75	1.35	0.7218	-1	HIRES
2451069.88122	-1.29	1.47	0.7261	-1	HIRES
2451075.80608	7.09	1.21	0.6631	-1	HIRES
2451341.05512	-7.35	1.52	0.6168	-1	HIRES
2451368.86865	-5.04	1.57	0.5584	-1	HIRES
2451409.92287	2.89	1.99	0.6589	-1	HIRES
2451439.81141	3.88	1.54	0.6635	-1	HIRES
2451439.81802	7.60	1.60	0.6523	-1	HIRES

(This table is available in its entirety in machine-readable form.)

Table 7
Radial Velocity Data for HD 216520

MJD	RV (m s ⁻¹)	σ_{RV} (m s ⁻¹)	S Index	H Index	Instrument
2452188.92575	-2.46	1.25	0.1696	-1	HIRES
2452189.85472	-0.41	1.49	0.185	-1	HIRES
2452235.68115	-1.11	1.38	0.1799	-1	HIRES
2452446.08978	1.34	1.37	0.1814	-1	HIRES
2452487.04685	-1.40	1.31	0.1802	-1	HIRES
2452487.93822	-3.99	1.32	0.171	-1	HIRES
2452488.96981	-2.27	1.25	0.1678	-1	HIRES
2452537.89594	-2.53	1.38	0.1747	-1	HIRES
2452574.81330	0.48	1.47	0.1363	-1	HIRES
2452833.03093	3.99	1.57	0.1383	-1	HIRES

(This table is available in its entirety in machine-readable form.)

Table 8
Radial Velocity Data for GJ 686

MJD	RV (m s ⁻¹)	σ_{RV} (m s ⁻¹)	S Index	H Index	Instrument
2453159.74925	3.65	0.95	0.54270	0.28195	TERRA
2453574.62254	0.81	0.82	0.67370	0.28953	TERRA
2453817.86816	-0.83	0.75	0.63931	0.29228	TERRA
2454174.87133	-1.72	0.77	0.63735	0.26124	TERRA
2454194.90763	2.51	0.78	0.73922	0.28956	TERRA
2454300.64483	-2.47	0.72	0.65581	0.28934	TERRA
2454948.86154	-1.17	0.57	0.66352	0.23889	TERRA
2454950.86206	-2.71	0.64	0.65440	0.23478	TERRA
2454956.83071	-0.53	0.88	0.56384	0.23619	TERRA
2455390.64094	1.13	1.10	0.67622	0.27807	TERRA

(This table is available in its entirety in machine-readable form.)

Table 9
Radial Velocity Data for HD 180617

MJD	RV (m s ⁻¹)	σ_{RV} (m s ⁻¹)	S Index	H Index	Instrument
2453159.81073	-1.89	0.68	0.93516	0.24810	TERRA
2453517.83909	1.13	0.67	1.08339	0.21657	TERRA
2453572.76530	1.38	1.52	1.15631	0.11502	TERRA
2453573.72190	-1.81	0.64	1.07858	0.19700	TERRA
2453574.68500	-1.82	0.41	1.11689	0.16847	TERRA
2453575.65016	-1.55	0.29	1.01041	0.21838	TERRA
2453576.65304	-2.48	0.75	1.00409	0.21559	TERRA
2453577.67857	-0.95	0.47	1.06946	0.19882	TERRA
2453578.67547	-1.44	0.37	0.99462	0.22405	TERRA
2453579.65731	-2.24	0.45	0.98758	0.23099	TERRA

(This table is available in its entirety in machine-readable form.)

ORCID iDs

Jennifer Burt  <https://orcid.org/0000-0002-0040-6815>
 Fabo Feng  <https://orcid.org/0000-0001-6039-0555>
 Bradford Holden  <https://orcid.org/0000-0002-6153-3076>
 Eric E. Mamajek  <https://orcid.org/0000-0003-2008-1488>
 Chelsea X. Huang  <https://orcid.org/0000-0003-0918-7484>
 Mickey M. Rosenthal  <https://orcid.org/0000-0003-3938-3099>
 Songhu Wang  <https://orcid.org/0000-0002-7846-6981>
 R. Paul Butler  <https://orcid.org/0000-0003-1305-3761>
 Steven S. Vogt  <https://orcid.org/0000-0001-7177-7456>
 Gregory Laughlin  <https://orcid.org/0000-0002-3253-2621>
 Gregory W. Henry  <https://orcid.org/0000-0003-4155-8513>
 Jeffrey D. Crane  <https://orcid.org/0000-0002-5226-787X>
 Steve A. Shectman  <https://orcid.org/0000-0002-8681-6136>

References

- Affer, L., Damasso, M., Micela, G., et al. 2019, *A&A*, **622**, A193
 Aguilera-Gómez, C., Ramírez, I., & Chanamé, J. 2018, *A&A*, **614**, A55
 Anders, F., Khalatyan, A., Chiappini, C., et al. 2019, *A&A*, **628**, A94
 Anglada-Escudé, G., & Butler, R. P. 2012, *ApJS*, **200**, 15
 Bai, Y., Liu, J., Bai, Z., Wang, S., & Fan, D. 2019, *AJ*, **158**, 93
 Baranne, A., Queloz, D., Mayor, M., et al. 1996, *A&AS*, **119**, 373
 Bayo, A., Rodrigo, C., Barrado Y Navascués, D., et al. 2008, *A&A*, **492**, 277
 Beatty, T. G., & Gaudi, B. S. 2015, *PASP*, **127**, 1240
 Bensby, T., Feltzing, S., & Oey, M. S. 2014, *A&A*, **562**, A71
 Bermejo, J. M., Asensio Ramos, A., & Allende Prieto, C. 2013, *A&A*, **553**, A95
 Bianchi, L., Shiao, B., & Thilker, D. 2017, *ApJS*, **230**, 24
 Biazzo, K., Frasca, A., Catalano, S., & Marilli, E. 2007, *AN*, **328**, 938
 Bland-Hawthorn, J., & Gerhard, O. 2016, *ARA&A*, **54**, 529
 Boeche, C., & Grebel, E. K. 2016, *A&A*, **587**, A2
 Bopp, B. W., & Espenak, F. 1977, *AJ*, **82**, 916
 Bouchy, F., Hébrard, G., Delfosse, X., et al. 2011, in EPSC-DPS Joint Meeting 2011 (Göttingen: Copernicus Gesellschaft mbH), 240
 Bouchy, F., Pepe, F., & Queloz, D. 2001, *A&A*, **374**, 733
 Bourges, L., Mella, G., Laffrasse, S., et al. 2017, *yCat*, **2346**, 0
 Bovy, J. 2016, *ApJ*, **817**, 49
 Brandt, T. D., & Huang, C. X. 2015, *ApJ*, **807**, 24
 Brewer, J. M., Fischer, D. A., Valenti, J. A., & Piskunov, N. 2016, *ApJS*, **225**, 32
 Brewer, J. M., Wang, S., Fischer, D. A., & Foreman-Mackey, D. 2018, *ApJL*, **867**, L3
 Bryan, M. L., Knutson, H. A., Fulton, B., et al. 2019, *AJ*, **157**, 52
 Buchhave, L. A., Dressing, C. D., Dumusque, X., et al. 2016, *AJ*, **152**, 160
 Burt, J., Holden, B., Hanson, R., et al. 2015, *JATIS*, **1**, 044003
 Burt, J. A., Nielsen, L. D., Quinn, S. N., et al. 2020, *AJ*, **160**, 153
 Butler, R. P., Marcy, G. W., Williams, E., et al. 1996, *PASP*, **108**, 500
 Butler, R. P., Vogt, S. S., Laughlin, G., et al. 2017, *AJ*, **153**, 208
 Cañas, C. I., Wang, S., Mahadevan, S., et al. 2019, *ApJL*, **870**, L17
 Casagrande, L., Portinari, L., & Flynn, C. 2006, *MNRAS*, **373**, 13
 Casagrande, L., Ramírez, I., Meléndez, J., Bessell, M., & Asplund, M. 2010, *A&A*, **512**, A54
 Chambers, J. E., Wetherill, G. W., & Boss, A. P. 1996, *Icar*, **119**, 261
 Chelli, A., Duvert, G., Bourguès, L., et al. 2016, *A&A*, **589**, A112
 Chen, Y., Girardi, L., Bressan, A., et al. 2014, *MNRAS*, **444**, 2525
 Christiansen, J. L., Vanderburg, A., Burt, J., et al. 2017, *AJ*, **154**, 122
 Cosentino, R., Lovis, C., Pepe, F., et al. 2012, *Proc. SPIE*, **8446**, 84461V
 Crane, J., Shectman, S. A., Butler, R. P., et al. 2010, *Proc. SPIE*, **7735**, 773553
 Crane, J. D., Shectman, S. A., & Butler, R. P. 2006, *Proc. SPIE*, **6269**, 626931
 Crane, J. D., Shectman, S. A., Butler, R. P., Thompson, I. B., & Burley, G. S. 2008, *Proc. SPIE*, **7014**, 701479
 Cummings, J. D., Deliyannis, C. P., Maderak, R. M., & Steinhauer, A. 2017, *AJ*, **153**, 128
 Curtis, J. L., Agüeros, M. A., Douglas, S. T., & Meibom, S. 2019, *ApJ*, **879**, 49
 Cutri, R. M., Skrutskie, M. F., van Dyk, S., et al. 2003, *yCat*, **2246**, 0
 Cutri, R. M., Wright, E. L., Conrow, T., et al. 2012, *yCat*, **2231**, 0
 Dawson, R. I., & Fabrycky, D. C. 2010, *ApJ*, **722**, 937
 Díaz, M. R., Jenkins, J. S., Tuomi, M., et al. 2018, *AJ*, **155**, 126
 Dumusque, X., Borsa, F., Damasso, M., et al. 2017, *A&A*, **598**, A133
 Duncan, D. K., Vaughan, A. H., Wilson, O. C., et al. 1991, *ApJS*, **76**, 383
 Dutra-Ferreira, L., Pasquini, L., Smiljanic, R., Porto de Mello, G. F., & Steffen, M. 2016, *A&A*, **585**, A75
 Egeland, R., Soon, W., Baliunas, S., et al. 2017, *ApJ*, **835**, 25
 Eker, Z., Bakış, V., Bilir, S., et al. 2018, *MNRAS*, **479**, 5491
 ESA 1997, in The Hipparcos Catalogue, Vol. 1–17 (Noordwijk: ESA)
 Díaz, F., Crane, J. D., Xuesong Wang, S., et al. 2019, *ApJS*, **242**, 25
 Feng, F., Tuomi, M., & Jones, H. R. A. 2017a, *A&A*, **605**, A103
 Feng, F., Tuomi, M., & Jones, H. R. A. 2017b, *MNRAS*, **470**, 4794
 Feng, F., Tuomi, M., Jones, H. R. A., Butler, R. P., & Vogt, S. 2016, *MNRAS*, **461**, 2440
 Franchini, M., Morossi, C., di Marcantonio, P., Malagnini, M. L., & Chavez, M. 2014, *MNRAS*, **442**, 220
 Frasca, A., Biazzo, K., Lanzafame, A. C., et al. 2015, *A&A*, **575**, A4
 Gagné, J., Mamajek, E. E., Malo, L., et al. 2018, *ApJ*, **856**, 23
 Gaia Collaboration, Brown, A. G. A., Vallenari, A., et al. 2016, *A&A*, **595**, A2
 Gaia Collaboration, Brown, A. G. A., Vallenari, A., et al. 2018, *A&A*, **616**, A1
 Gladman, B. 1993, *Icar*, **106**, 247
 Gomes da Silva, J., Santos, N. C., Bonfils, X., et al. 2011, *A&A*, **534**, A30
 Gomes da Silva, J., Santos, N. C., Bonfils, X., et al. 2012, *A&A*, **541**, A9
 González Hernández, J. I., & Bonifacio, P. 2009, *A&A*, **497**, 497
 Gossage, S., Conroy, C., Dotter, A., et al. 2018, *ApJ*, **863**, 67
 Gray, R. O., Corbally, C. J., Garrison, R. F., et al. 2006, *AJ*, **132**, 161
 Gray, R. O., Corbally, C. J., Garrison, R. F., McFadden, M. T., & Robinson, P. E. 2003, *AJ*, **126**, 2048
 Guo, X., Johnson, J. A., Mann, A. W., et al. 2017, *ApJ*, **838**, 25
 Haario, H., Laine, M., Mira, A., & Saksman, E. 2006, *Stat. Comput.*, **16**, 339
 Hadden, S., & Lithwick, Y. 2017, *AJ*, **154**, 5
 Henry, G. W. 1999, *PASP*, **111**, 845
 Henry, G. W., Marcy, G., Butler, R. P., & Vogt, S. S. 1999, *IAUC*, **7307**, 1
 Henry, G. W., Marcy, G. W., Butler, R. P., & Vogt, S. S. 2000, *ApJL*, **529**, L41
 Hinkel, N. R., Mamajek, E. E., Turnbull, M. C., et al. 2017, *ApJ*, **848**, 34
 Houdebine, E. R. 2012, *MNRAS*, **421**, 3189
 Houdebine, É. R., Mullan, D. J., Doyle, J. G., et al. 2019, *AJ*, **158**, 56
 Houdebine, E. R., Mullan, D. J., Paletou, F., & Gebran, M. 2016, *ApJ*, **822**, 97
 Howard, A. W., Johnson, J. A., Marcy, G. W., et al. 2010, *ApJ*, **721**, 1467

- Isaacson, H., & Fischer, D. 2010, *ApJ*, **725**, 875
- Jenkins, J. M., Twicken, J. D., McCauliff, S., et al. 2016, *Proc. SPIE*, **9913**, 99133E
- Kaminski, A., Trifonov, T., Caballero, J. A., et al. 2018, *A&A*, **618**, A115
- Kass, R. E., & Raftery, A. E. 1995, *J. Am. Stat. Assoc.*, **90**, 773
- Katz, D., Soubiran, C., Cayrel, R., et al. 2011, *A&A*, **525**, A90
- Kazarovets, E. V., Kireeva, N. N., Samus, N. N., & Durlevich, O. V. 2003, *IBVS*, **5422**, 1
- Kervella, P., Arenou, F., Mignard, F., & Thévenin, F. 2019, *A&A*, **623**, A72
- Kóspál, Á, Ardila, D. R., Moór, A., & Ábrahám, P. 2009, *ApJL*, **700**, L73
- Lalitha, S., Baroch, D., Morales, J. C., et al. 2019, *A&A*, **627**, A116
- Latham, D. W., Rowe, J. F., Quinn, S. N., et al. 2011, *ApJL*, **732**, L24
- Lépine, S., & Gaidos, E. 2011, *AJ*, **142**, 138
- Lépine, S., Hilton, E. J., Mann, A. W., et al. 2013, *AJ*, **145**, 102
- Liddle, A. R. 2007, *MNRAS*, **377**, L74
- Lindgren, L., Hernández, J., Bombrun, A., et al. 2018, *A&A*, **616**, A2
- Lissauer, J. J., Dawson, R. I., & Tremaine, S. 2014, *Natur*, **513**, 336
- Lissauer, J. J., Ragozzine, D., Fabrycky, D. C., et al. 2011, *ApJS*, **197**, 8
- Liu, F., Yong, D., Asplund, M., Ramírez, I., & Meléndez, J. 2016, *MNRAS*, **457**, 3934
- Lockwood, G. W., Skiff, B. A., & Radick, R. R. 1997, *ApJ*, **485**, 789
- Lodieu, N., Pérez-Garrido, A., Smart, R. L., & Silvotti, R. 2019, *A&A*, **628**, A66
- López-Morales, M., Morrell, N. I., Butler, R. P., & Seager, S. 2006, *PASP*, **118**, 1506
- Luck, R. E. 2017, *AJ*, **153**, 21
- Luck, R. E., & Heiter, U. 2005, *AJ*, **129**, 1063
- Mackereth, J. T., & Bovy, J. 2018, *PASP*, **130**, 114501
- Mamajek, E. E., & Hillenbrand, L. A. 2008, *ApJ*, **687**, 1264
- Mann, A. W., Feiden, G. A., Gaidos, E., Boyajian, T., & von Braun, K. 2015, *ApJ*, **804**, 64
- Martín, E. L., Lodieu, N., Pavlenko, Y., & Béjar, V. J. S. 2018, *ApJ*, **856**, 40
- Mayor, M., Pepe, F., Queloz, D., et al. 2003, *Msngr*, **114**, 20
- Meschiari, S., Wolf, A. S., Rivera, E., et al. 2009, *PASP*, **121**, 1016
- Mikolaitis, Š., Drazdauskas, A., Minkevičiūtė, R., et al. 2019, *A&A*, **628**, A49
- Millholland, S., Wang, S., & Laughlin, G. 2017, *ApJL*, **849**, L33
- Mishenina, T. V., Pignatari, M., Korotín, S. A., et al. 2013, *A&A*, **552**, A128
- Mishenina, T. V., Soubiran, C., Bienaymé, O., et al. 2008, *A&A*, **489**, 923
- Mishenina, T. V., Soubiran, C., Kovtyukh, V. V., Katsova, M. M., & Livshits, M. A. 2012, *A&A*, **547**, A106
- Nelson, B. E., Ford, E. B., Buchner, J., et al. 2020, *AJ*, **159**, 73
- Ning, B., Wolfgang, A., & Ghosh, S. 2018, *ApJ*, **869**, 5
- Olsper, N., Lehtinen, J. J., Kämpylä, M. J., Pelt, J., & Grigorievskiy, A. 2018, *A&A*, **619**, A6
- Pepe, F., Mayor, M., Queloz, D., et al. 2004, *A&A*, **423**, 385
- Pepe, F., Mayor, M., Rupprecht, G., et al. 2002, *Msngr*, **110**, 9
- Perryman, M. 2011, *The Exoplanet Handbook* (Cambridge: Cambridge Univ. Press)
- Pinamonti, M., Sozzetti, A., Giacobbe, P., et al. 2019, *A&A*, **625**, A126
- Quirrenbach, A., Amado, P. J., Caballero, J. A., et al. 2014, *Proc. SPIE*, **9147**, 91471F
- Quirrenbach, A., Amado, P. J., Seifert, W., et al. 2018, *Proc. SPIE*, **8446**, 84460R
- Radick, R. R., Lockwood, G. W., Skiff, B. A., & Baliunas, S. L. 1998, *ApJS*, **118**, 239
- Rajpaul, V., Aigrain, S., & Roberts, S. 2016, *MNRAS*, **456**, L6
- Ramírez, I., Fish, J. R., Lambert, D. L., & Allende Prieto, C. 2012, *ApJ*, **756**, 46
- Rein, H., & Liu, S. F. 2012, *A&A*, **537**, A128
- Rein, H., & Tamayo, D. 2015, *MNRAS*, **452**, 376
- Reiners, A., Zechmeister, M., Caballero, J. A., et al. 2018, *A&A*, **612**, A49
- Ricker, G. K., Winn, J. N., Vanderspek, R., et al. 2014, *Proc. SPIE*, **9143**, 920
- Rowan, D., Meschiari, S., Laughlin, G., et al. 2016, *ApJ*, **817**, 104
- Rowe, J. F., Bryson, S. T., Marcy, G. W., et al. 2014, *ApJ*, **784**, 45
- Schweitzer, A., Passegger, V. M., Cifuentes, C., et al. 2019, *A&A*, **625**, A68
- Slocum, F., & Mitchell, S. A. 1913, *ApJ*, **38**, 1
- Smith, J. C., Stumpe, M. C., Van Cleve, J. E., et al. 2012, *PASP*, **124**, 1000
- Soubiran, C., Jasiewicz, G., Chemin, L., et al. 2013, *A&A*, **552**, A64
- Stassun, K. G., Oelkers, R. J., Paegert, M., et al. 2019, *AJ*, **158**, 138
- Sickler, J. K., Wang, S., Wolfgang, A., et al. 2018, *AJ*, **156**, 102
- Steffen, J. H., Ragozzine, D., Fabrycky, D. C., et al. 2012, *PNAS*, **109**, 7982
- Stevens, D. J., Stassun, K. G., & Gaudi, B. S. 2017, *AJ*, **154**, 259
- Stumpe, M. C., Smith, J. C., Catanzarite, J. H., et al. 2014, *PASP*, **126**, 100
- Stumpe, M. C., Smith, J. C., Van Cleve, J. E., et al. 2012, *PASP*, **124**, 985
- Suárez Mascareño, A., Rebolo, R., González Hernández, J. I., & Esposito, M. 2017, *MNRAS*, **468**, 4772
- Takeda, G., Ford, E. B., Sills, A., et al. 2007, *ApJS*, **168**, 297
- Teske, J. K., Wang, S., Wolfgang, A., et al. 2018, *AJ*, **155**, 148
- Torres, G. 2010, *AJ*, **140**, 1158
- Torres, G. 2019, *ApJ*, **883**, 105
- Tuomi, M., Jones, H. R. A., Barnes, J. R., et al. 2018, *AJ*, **155**, 192
- Tuomi, M., Jones, H. R. A., Jenkins, J. S., et al. 2013, *A&A*, **551**, A79
- Van Eylen, V., & Albrecht, S. 2015, *ApJ*, **808**, 126
- Vanderburg, A., & Johnson, J. A. 2014, *PASP*, **126**, 948
- Vican, L. 2012, *AJ*, **143**, 135
- Vogt, S. S., Allen, S. L., Bigelow, B. C., et al. 1994, *Proc. SPIE*, **2198**, 362
- Vogt, S. S., Butler, R. P., Burt, J., et al. 2017, *AJ*, **154**, 181
- Vogt, S. S., Radovan, M., Kibrick, R., et al. 2014, *PASP*, **126**, 359
- Wang, S. 2017, *RNAAS*, **1**, 26
- Wang, S., Addison, B., Fischer, D. A., et al. 2018, *AJ*, **155**, 70
- Weiss, L. M., Marcy, G. W., Petigura, E. A., et al. 2018, *AJ*, **155**, 48
- Winn, J. N. 2010, in *Exoplanets*, ed. S. Seager (Tucson, AZ: Univ. Arizona Press), **55**
- Winn, J. N., & Fabrycky, D. C. 2015, *ARA&A*, **53**, 409
- Wright, J. T., Marcy, G. W., Butler, R. P., & Vogt, S. S. 2004, *ApJS*, **152**, 261
- Wright, N. J., Drake, J. J., Mamajek, E. E., & Henry, G. W. 2011, *ApJ*, **743**, 48
- Zechmeister, M., Reiners, A., Amado, P. J., et al. 2018, *A&A*, **609**, A12